

Targeting renal tubular WWP2 to restore mitochondrial OXPHOS integrity retards the AKI-to-CKD transition

Mengqiu Wu,^{1,2,3,5} Mengqiu Miao,^{1,2,3,5} Yuting Li,^{1,2,3,5} Jiaojiao Fan,^{1,2,3} Wenping Zhu,^{1,2,3} Yujia Niu,^{1,2,3} Ruotian Liu,^{2,3} Weiyi Chen,^{1,2,3,4} Ran Zou,^{2,3} Songming Huang,^{1,2,3} Yue Zhang,^{1,2,3} Mi Bai,^{1,2,3} Ran You,^{1,2,3} Zhanjun Jia,^{1,2,3} and Aihua Zhang^{1,2,3}

¹Department of Nephrology, State Key Laboratory of Reproductive Medicine, Children's Hospital of Nanjing Medical University, Nanjing 211166, China; ²Jiangsu Key Laboratory of Pediatrics, Nanjing Medical University, Nanjing 210029, China; ³Nanjing Key Laboratory of Pediatrics, Children's Hospital of Nanjing Medical University, Nanjing 210008, China; ⁴Department of Emergency/Critical Medicine, Children's Hospital of Nanjing Medical University, Nanjing 210008, China

Defects in mitochondrial energy metabolism in injured tubular epithelial cells (TECs) are a well-recognized hallmark of kidney injury pathogenesis; however, the key target leading to this defect during the acute kidney injury (AKI)-to-chronic kidney disease (CKD) transition remains elusive. Here, we found that during the AKI-to-CKD transition, the increased WW domain containing E3 ubiquitin protein ligase 2 (WWP2) was shuttled to the mitochondria and disabled TEC mitochondrial energy metabolism by ubiquitinating and degrading complex II subunit succinate dehydrogenase complex subunit C (SDHC), leading to oxidative phosphorylation (OXPHOS) disability and aggravated TEC maladaptive repair. Preemptive and late depletion of *Wwp2* both ameliorated unilateral ischemia-reperfusion (UIR) injury-induced AKI-to-CKD transition, and tubular-specific *Wwp2* depletion resulted in the same protective phenotype. Furthermore, *Sdhc* knock-down abolished the protective effects of *Wwp2* deletion in UIR mice. Conversely, SDHC overexpression attenuated OXPHOS impairment and TEC injury following WWP2 overexpression. Finally, we leveraged high-throughput virtual screening, enzyme activity assays, and binding affinity assays to identify two candidate WWP2 inhibitors. Both inhibitors significantly improved TEC maladaptive repair and deferred the AKI-to-CKD transition. Overall, we identified WWP2 as a critical regulator of mitochondrial OXPHOS integrity in maladaptive repairing TECs and identified two WWP2 inhibitors as potential drug candidates for interrupting the AKI-to-CKD transition.

INTRODUCTION

Acute kidney injury (AKI) is a group of clinical syndromes characterized by rapid kidney function deterioration and is a global public health concern affecting 20.0%–31.7% of inpatients and 8.3% of outpatients.¹ With advances in medical healthcare, hemodynamic management (e.g., adequate hydration), glucocorticoid therapy, and renal replacement therapy have efficiently decreased the mortality

rate of AKI patients.² However, AKI survivors are at high risk for progressing to chronic kidney disease (CKD), which is referred to as the AKI-to-CKD transition.³

The renal proximal tubule is the main injury site during AKI.⁴ Previously, it was thought that injured tubular epithelial cells (TECs) could proliferate to regenerate functional TECs⁵; however, this hypothesis is inconsistent with the high incidence of CKD after AKI,³ and regeneration is rarely complete. Recent single-cell RNA sequence-based studies have revealed that a cluster of TECs undergoes maladaptive repair. This TEC subpopulation harbors abundant expression of proinflammatory and profibrotic genes and is engaged in paracrine signaling pathways, enhancing interstitial inflammation, fibroblast activation, and subsequent fibrotic remodeling.^{6–8} Thus, defining the molecular mechanisms underlying the maladaptive repair of TECs is critical for developing effective treatments against the AKI-to-CKD transition.

Mitochondria are the main biofuel source for cells, generating adenosine triphosphate (ATP) mainly through oxidative phosphorylation

Received 4 June 2025; accepted 13 November 2025;
<https://doi.org/10.1016/j.ymthe.2025.11.022>

⁵These authors contributed equally

Correspondence: Mi Bai, Department of Nephrology, State Key Laboratory of Reproductive Medicine, Children's Hospital of Nanjing Medical University, Nanjing 211166, China.

E-mail: baimi3@njmu.edu.cn

Correspondence: Ran You, Department of Nephrology, State Key Laboratory of Reproductive Medicine, Children's Hospital of Nanjing Medical University, Nanjing 211166, China.

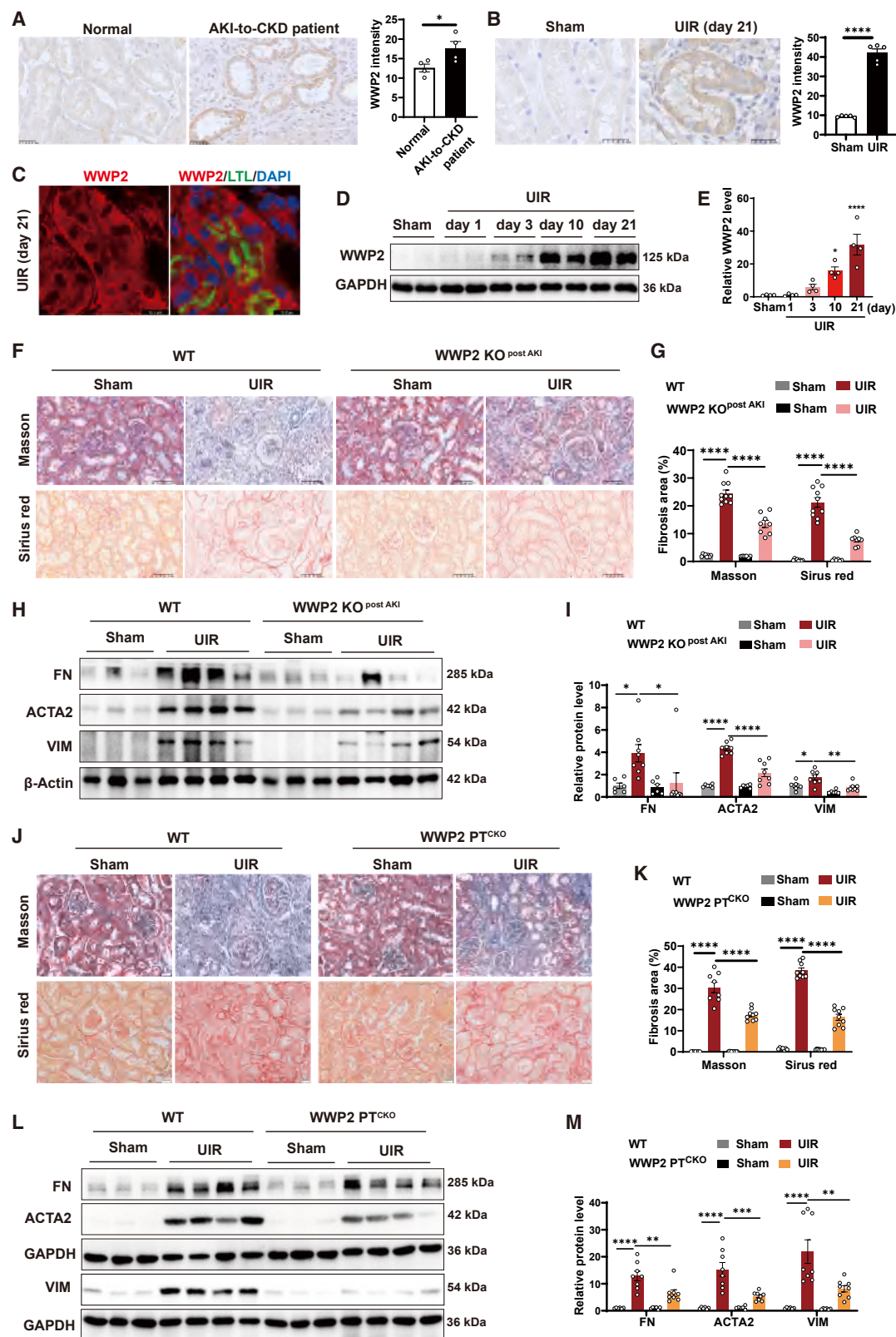
E-mail: yourannch@njmu.edu.cn

Correspondence: Zhanjun Jia, Department of Nephrology, State Key Laboratory of Reproductive Medicine, Children's Hospital of Nanjing Medical University, Nanjing 211166, China.

E-mail: jiazhazhanjun72@njmu.edu.cn

Correspondence: Aihua Zhang, Department of Nephrology, State Key Laboratory of Reproductive Medicine, Children's Hospital of Nanjing Medical University, Nanjing 211166, China.

E-mail: zhaihua@njmu.edu.cn



(legend on next page)

(OXPHOS). Defects in mitochondrial energy production in TECs, characterized by impaired fatty acid β -oxidation (FAO) and enhanced glycolysis, are well-recognized hallmarks in the pathobiology of AKI and CKD.^{9,10} Recently, studies have also indicated that mitochondrial energy production disorder, accompanied by increased mitochondrial oxygen free radical generation, may hinder TEC regeneration and increase the risk of the AKI-to-CKD transition.^{11–13} However, the key element leading to persistent mitochondrial energy production dysfunction during the AKI-to-CKD transition remains elusive.

WW domain-containing E3 ubiquitin protein ligase 2 (WWP2), a member of the neuronally expressed developmentally down-regulated 4 (Nedd4) family, has been proved to be a critical regulator of cellular homeostasis. In normal conditions, WWP2 plays critical roles in regulating cell genomic integrity, proliferation, and stress response. WWP2 protects genomic integrity by ubiquitinating and facilitating the degradation of RNA polymerase II, thereby protecting cells from double-strand breaks (DSBs).¹⁴ WWP2 could attenuate oxidative stress by suppressing reactive oxygen species (ROS) generation and apoptosis.¹⁵ WWP2 also promotes T cell proliferation by catalyzing early growth response protein 2 (EGR2) ubiquitination and degradation.¹⁶ However, WWP2 has also been reported to play pathological roles in mediating tumor progression,^{17,18} cardiac hypertrophy, and fibrosis.^{19,20} In this study, we found for the first time that during the AKI-to-CKD transition, the continuously increased WWP2 entered the mitochondria and mediated TEC mitochondrial energy production defects via ubiquitination and degradation of succinate dehydrogenase complex subunit C (SDHC), a core subunit of the complex II (also known as succinate dehydrogenase complex). Moreover, on the basis of our functional and mechanistic studies, we conducted high-throughput virtual screening, WWP2 ubiquitylation enzyme activity assays, and binding affinity assays to identify WWP2 inhibitors. Two candidate molecules possessing WWP2 inhibitory capability and binding affinity were selected, and both could significantly attenuate TEC

maladaptive repair and interrupt the AKI-to-CKD transition. In summary, we confirmed WWP2 as a promising therapeutic target for intervention the AKI-to-CKD transition and identified H36-E4 and H111-H7 as potential candidates for further drug development.

RESULTS

Tubular expression of WWP2 increased during the AKI-to-CKD transition

First, we investigated the expression of WWP2 in AKI-to-CKD transition patients. Kidney biopsies from four CKD patients with a history of AKI were used for WWP2 immunostaining. The clinical parameters of the patients included are shown in Table S1. The results revealed that WWP2 is significantly elevated in AKI-to-CKD transition patients, with the signal located predominantly in the renal tubules (Figure 1A). Second, we established AKI-to-CKD transition models via unilateral kidney ischemia-reperfusion (UIR) injury and repeated low-dose cisplatin (repeated-CP) stimuli in mice.^{21,22} In UIR mouse kidneys, elevated expression of WWP2 in the renal tubules was also observed via immunostaining (Figures 1B and 1C); time-lapse western blotting revealed that WWP2 expression gradually increased with the progression from AKI to CKD after UIR injury (Figures 1D and 1E). In repeated-CP injured mice kidneys, WWP2 expression was also significantly elevated (Figure S1).

In vitro, mouse proximal tubule cells (mPTCs) were first exposed to hypoxia (1% O₂) for 12 h, followed by reoxygenation and transforming growth factor β 1 (TGF- β 1) treatment for another 24 h (referred to as H/R + T stimuli) (Figure S2A). After H/R + T stimuli, mPTCs exhibited maladaptive repair, with significantly elevated expression of early DSB marker phosphorylated histone H₂AX (p-H₂AX) and transdifferentiation markers (fibronectin [FN] and actin alpha 2 [ACTA2]) (Figures S2B and S2C). Interestingly, the expression of WWP2 within maladaptively repaired mPTCs was also gradually increased (Figures S2B and S2D), recapitulating the murine model

Figure 1. Wwp2 ablation attenuated the ischemia-induced AKI-to-CKD transition

(A) Representative immunohistochemical staining and quantitative analysis of WWP2 expression in nondiseased portions of the kidney from renal cell carcinoma patients and kidney sections of AKI-to-CKD patients from the Department of Nephrology, Children's Hospital of Nanjing Medical University. Scale bar, 25 μ m. Bars represent quantification results (mean \pm SEM, n = 4 patients for each group). (B) Representative immunohistochemical staining and quantitative analysis of WWP2 expression in day 21 UIR mouse kidneys. Scale bar, 25 μ m. Bars represent quantification results (mean \pm SEM, n = 5 mice for each group). (C) Representative immunofluorescent staining of WWP2 expression in day 21 UIR mouse kidneys. Scale bar, 12.3 μ m. (D and E) Time-lapse western blotting analysis and semiquantification of WWP2 expression in UIR mouse kidneys. Bars represent quantification results (mean \pm SEM, n = 4 mice for each group). (F and G) Tamoxifen-inducible *Wwp2* knockout mice (WWP2 iKO) and control mice (WT) were subjected to UIR modeling, with tamoxifen injected 3 days postreperfusion to initiate *Wwp2* gene depletion (WWP2 KO^{post AKI}). Masson's trichrome staining and Sirius red staining were performed to assess the extent of kidney fibrosis in the different groups. Scale bar, 50 μ m. Bars represent quantification results (mean \pm SEM, n = 8 mice for WT sham and WWP2 KO^{post AKI} UIR groups, n = 10 mice for the WT UIR group, n = 6 mice for the WWP2 KO^{post AKI} sham group). (H and I) Representative western blot images and summary data showing the relative protein levels of FN, ACTA2, and VIM in whole-kidney protein lysates from different groups. Bars represent quantification results (mean \pm SEM, n = 6 mice for the WT sham and WWP2 KO^{post AKI} sham groups, and n = 8 mice for the WT UIR and WWP2 KO^{post AKI} UIR groups). (J and K) Tubule-specific *Wwp2* KO (WWP2 PT^{CKO}) mice and WT mice were subjected to UIR modeling. Masson's trichrome staining and Sirius red staining were performed to assess the extent of kidney fibrosis in the different groups. Scale bar, 20 μ m. Bars represent quantification results (mean \pm SEM, n = 7 mice for the WT sham group, n = 8 mice for the WT UIR group, n = 10 mice for the WWP2 PT^{CKO} sham group, and n = 9 mice for the WWP2 PT^{CKO} UIR group). (L and M) Representative western blot images and summary data showing the relative protein levels of FN, ACTA2, and VIM in whole-kidney protein lysates from different groups. Bars represent quantification results (mean \pm SEM, n = 6 mice for the WT sham and WWP2 PT^{CKO} sham groups, and n = 8 mice for the WT UIR and WWP2 PT^{CKO} UIR groups). An unpaired Student's *t* test was used to assess the statistical significance of differences between two groups for (A) and (B). One-way ANOVA was used to assess the statistical significance of differences between groups for (E). Two-way ANOVA was used to determine the *p* values for (G), (I), (K), and (M). **p* < 0.05; ***p* < 0.01; ****p* < 0.001; *****p* < 0.0001.

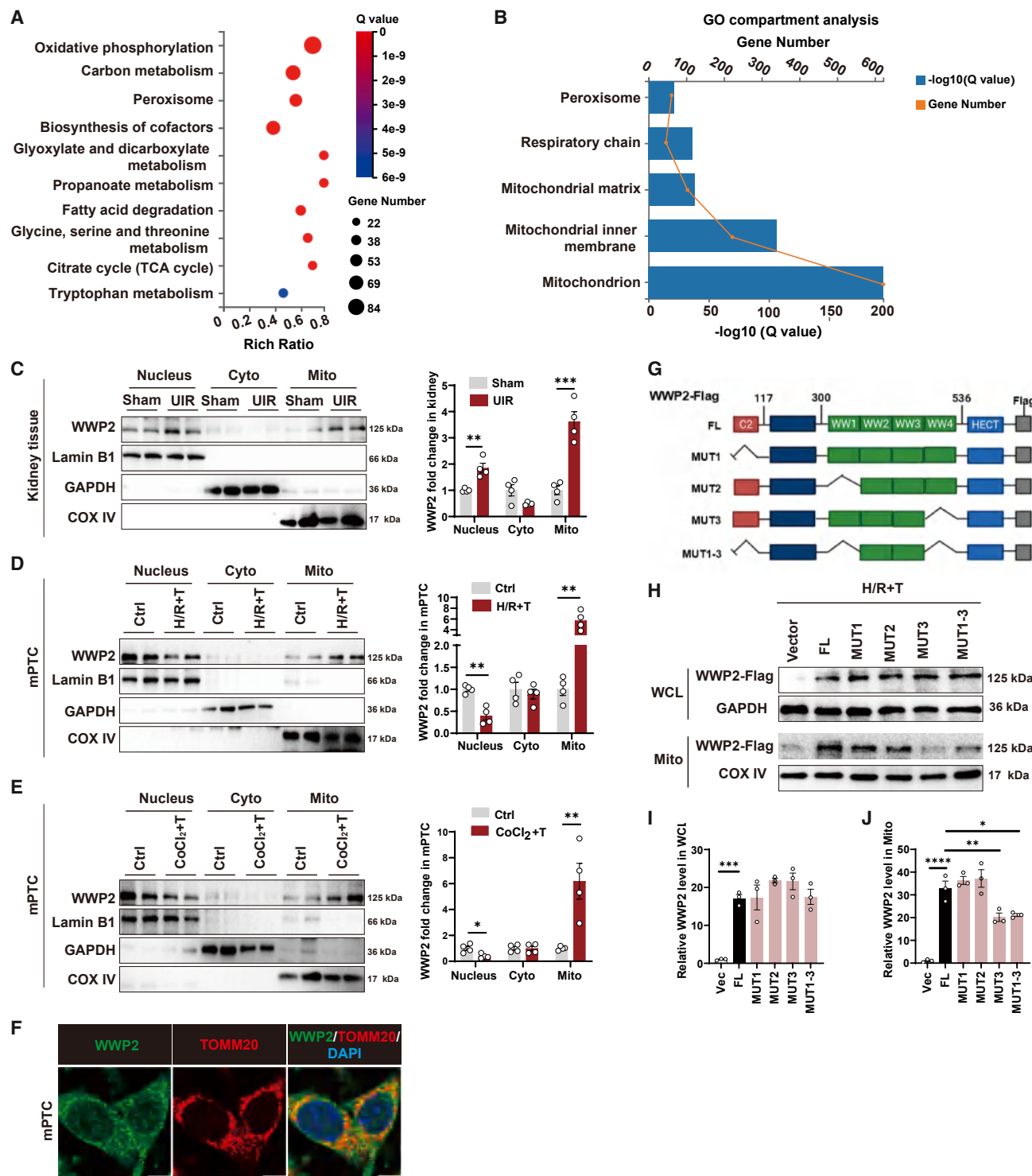


Figure 2. Tubular WWP2 protein was enriched in mitochondria during the AKI-to-CKD transition

(A) An unbiased RNA-seq analysis was performed with mouse kidney tissues. Genes concurrently downregulated in the UIR group and restored by WWP2 PT^{CKO} were subjected to KEGG analysis. (B) GO cell compartment analysis revealed that the genes were predominantly enriched in the mitochondrion and respiratory chain categories. (C) Representative Western blot images and summary data of the relative protein levels of WWP2 in the nucleus, cytoplasm (Cyto), and mitochondria (Mito) of day 21 UIR kidney tissues are shown. Bars represent quantification results (mean \pm SEM, $n = 4$ mice for each group). (D) mPTCs were subjected to hypoxia (1% O₂) for 12 h, followed by

(legend continued on next page)

findings. We also treated cells with CoCl_2 for 12 h to induce chemical hypoxia, followed by washouts and TGF- β 1 treatment for 24 h (referred to as CoCl_2 + T treatment) (Figure S2E). Similar to our observations in mPTCs treated with H/R + T stimuli, mPTCs with CoCl_2 + T treatment also exhibited maladaptive repair and increased expression of WWP2 (Figures S2F and S2G). These results imply that hypoxia + TGF- β 1-treated mPTCs represent a reliable *in vitro* model for studying the AKI-to-CKD transition, which mimic acute ischemia injury and increased TGF- β 1 levels within the tissue during the postinjury phase. Together, these data demonstrate increased tubular expression of WWP2 during the AKI-to-CKD transition.

Depletion of *Wwp2* before or after the acute phase attenuated the AKI-to-CKD transition

Previously, our team reported that *Wwp2* knockout (WWP2 KO) aggravated renal function in cisplatin induced AKI to some extent.²³ In the present study, we aimed to address the role of WWP2 during the AKI-to-CKD transition. We generated tamoxifen-inducible *Wwp2* knockout (WWP2 iKO) mice by crossbreeding *Wwp2*^{fl/fl} and CAG-CreERT2 mice. When tamoxifen was administered for 5 consecutive days, WWP2 in the kidneys of WWP2 iKO mice was almost completely ablated compared with that in the kidneys of *Wwp2*^{fl/fl} mice (wild-type [WT] littermates) (Figure S3A). To verify the role of WWP2 in the AKI-to-CKD transition, we injected tamoxifen 3 days postreperfusion after the AKI phase to initiate *Wwp2* gene depletion (WWP2 KO^{post AKI}). Kidney injury and fibrosis levels were evaluated on day 28 after UIR injury. Masson and Sirius red staining revealed that while WT mice exhibited remarkable flattening and sloughing of tubular epithelial cells, the tubular injury of WWP2 KO^{post AKI} mice was dramatically ameliorated (Figure 1F). Moreover, WT mice presented noticeable interstitial matrix deposits, which were also significantly alleviated in WWP2 KO^{post AKI} mice (Figures 1F and 1G). Similarly, the protein expression of fibrotic markers (FN, ACTA2, and vimentin [VIM]) was significantly lower in WWP2 KO^{post AKI} UIR mice than in WT UIR mice (Figures 1H and 1I). In addition, we knocked out *Wwp2* before ischemia injury (WWP2 KO^{before AKI}) and analyzed its long-term influence (Figure S3B). Masson staining, Sirius red staining, and western blotting of fibrotic markers validated similar renoprotective effects in WWP2 KO^{before AKI} mice (Figures S3C–S3F). By utilizing inducible global *Wwp2*-knockdown mice, we found that *Wwp2* depletion before or after the acute phase of AKI had a protective effect against the AKI-to-CKD transition.

Tubular-specific *Wwp2* deficiency retarded the AKI-to-CKD transition

Since tubular cells are the primary target of AKI and the main participants in the AKI-to-CKD transition,⁴ we next aimed to address the role of tubular cell WWP2 in the present experimental setting. Proximal tubule conditional *Wwp2* KO (WWP2 PT^{CKO}) mice were generated by crossing *Wwp2*^{fl/fl} mice with kidney androgen-regulated protein-Cre, as described previously.²³ WWP2 PT^{CKO} and WT mice were then subjected to UIR modeling. Masson and Sirius red staining revealed that tubulointerstitial fibrosis in UIR mice was significantly alleviated in the WWP2 PT^{CKO} group compared with that in the WT group (Figures 1J and 1K). Consistently, tubular-specific ablation of *Wwp2* also reduced the protein levels of FN, ACTA2, and VIM in UIR kidneys (Figures 1L and 1M). These results indicated that upregulated WWP2 expression in TECs could promote the AKI-to-CKD transition.

Tubular WWP2 is shuttled to the mitochondria during the AKI-to-CKD transition

To decipher the potential mechanism underlying the role of WWP2, the kidney tissues of WT and WWP2 PT^{CKO} mice with or without UIR injury were subjected to transcriptome analysis. Interestingly, genes that were concurrently downregulated in the UIR group and efficiently restored by WWP2 PT^{CKO} were significantly enriched in the OXPHOS, carbon metabolism, biosynthesis of cofactors, fatty acid degradation, and tricarboxylic acid (TCA) cycle pathways (Figure 2A). Gene Ontology (GO) enrichment analysis again highlighted the significant impact of WWP2 on mitochondria and the respiratory chain (Figure 2B). These unbiased data indicated the role of WWP2 in regulating mitochondria and OXPHOS function.

To determine the exact regulatory effect of WWP2 on mitochondria, we first estimated the subcellular localization of the increased WWP2 protein. In day 21 UIR mouse kidney tissues, both the nucleus and the mitochondrial WWP2 levels increased, with a greater fold change in the mitochondrial WWP2 (Figure 2C). *In vitro*, H/R + T- and CoCl_2 + T-challenged mPTCs exhibited a robust increase in mitochondrial WWP2 and a significant decrease in nuclear WWP2 (Figures 2D and 2E). The immunofluorescence study again revealed the dominant expression of WWP2 in the mitochondria (marked by TOMM20) of H/R + T-challenged mPTCs (Figure 2F). In contrast, the expression of WWP2 in the interstitial fibroblast line NRK-49F was increased in both the nucleus and the mitochondria (Figure S4). We then conducted time-lapse western blotting of

reoxygenation and stimulation with TGF- β 1 (5 $\mu\text{g/mL}$) for another 24 h (H/R + T). Representative western blot images and summary data showing the relative protein levels of WWP2 in the nucleus, cytoplasm, and mitochondria. Bars represent quantification results (mean \pm SEM, $n = 4$ independent experiments). (E) mPTCs were treated with CoCl_2 (200 nM) for 12 h to induce chemical hypoxia, followed by TGF- β 1 treatment for 24 h (CoCl_2 + T). Representative western blot images and summary data of the relative protein levels of WWP2 in the nucleus, cytoplasm, and mitochondria are shown. Bars represent quantification results (mean \pm SEM, $n = 4$ independent experiments). (F) Representative immunofluorescence co-staining of WWP2 and the mitochondrial marker TOMM20 in H/R + T-challenged mPTCs. Scale bar, 7.4 μm . (G) Schematic of four IMTS-L truncated mutants of WWP2. (H–J) mPTCs were transfected with a full-length (FL) WWP2-FLAG-tagged expression plasmid or truncated mutants of the WWP2-FLAG-tagged expression plasmids and then subjected to H/R + T. Western blotting was used to assess the expression of the fusion protein in whole-cell lysates (WCL) and mitochondria (Mito) with an anti-FLAG antibody. Bars represent quantification results (mean \pm SEM, $n = 3$ independent experiments). An unpaired Student's *t* test was used to assess the statistical significance of differences between two groups for (C)–(E). One-way ANOVA was used to assess the statistical significance of differences between groups for (I) and (J). * $p < 0.05$; ** $p < 0.01$; *** $p < 0.001$; **** $p < 0.0001$.

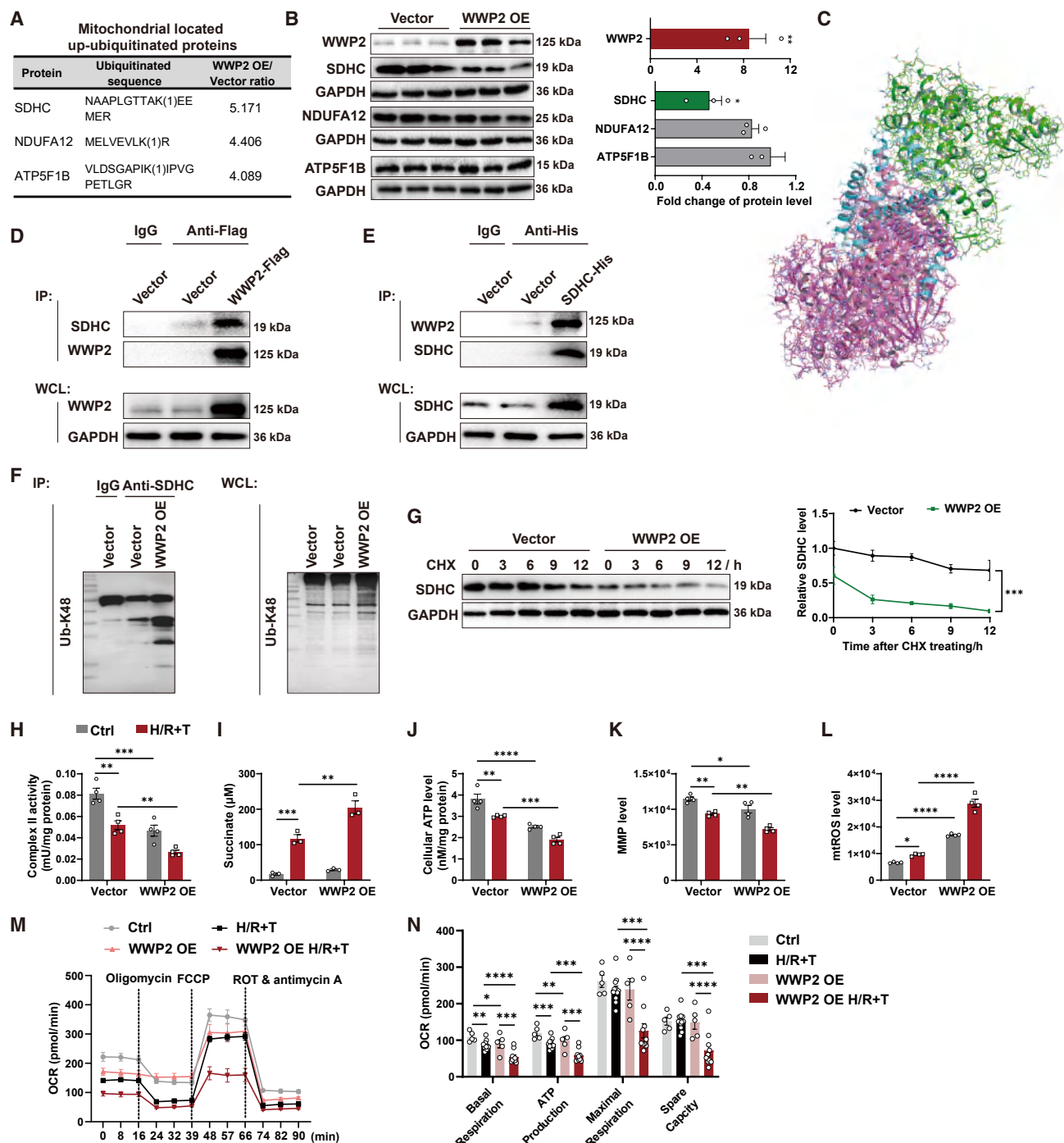


Figure 3. Elevated WWP2 targets the SDHC for polyubiquitylation and thus destroys OXPHOS in TECs

(A) *Wwp2*-FLAG was transfected into mPTCs for 24 h before the cells were collected for ubiquitylation-omics analysis. The mitochondrion-localized proteins that are increasingly ubiquitylated are listed. (B) Western blotting and quantitative analyses of WWP2, SDHC, NDUFA12, and ATP5F1B expression in WWP2-overexpressing mPTCs. Bars represent quantification results (mean \pm SEM, $n = 3$ independent experiments). (C) Molecular docking of the WWP2 HECT domain (PDB: 4Y07) and complex II (PDB: 8GS8). Green: WWP2; blue: SDHC subunit; pink: other subunits of complex II. (D) Vectors or FLAG-tagged *Wwp2* overexpression plasmids were transfected into mPTCs for 24 h, and the resulting cell lysate was subjected to an immunoprecipitation assay with an anti-FLAG antibody. Anti-IgG served as a negative control. Immunoprecipitation demonstrated that WWP2-FLAG binds to SDHC. (E) Vectors or His-tagged *Sdhc* overexpression plasmids were transfected into mPTCs for 24 h, and the cell lysate was subjected to an immunoprecipitation assay with an anti-His antibody. Anti-IgG served as a negative control. Immunoprecipitation demonstrated that SDHC-His binds to

(legend continued on next page)

nuclear and mitochondrial WWP2 expression in UIR kidneys, revealing that nuclear WWP2 showed late-onset enhancement (10 days postinjury), corresponding to the period of extensive myofibroblast proliferation and renal fibrosis (Figures S5A and S5B). In contrast, mitochondrial WWP2 increased at an earlier phase (3 days postinjury), corresponding to the time point of the AKI-to-CKD transition (Figures S5A and S5C). Thus, we speculated that the increased WWP2 expression within the mitochondria of TECs might be a key mediator of the AKI-to-CKD transition.

We then used the TargetP algorithm to predict the internal mitochondrial targeting sequence-like sequences (iMTS-Ls) within the mouse WWP2 protein.^{24,25} Three potential iMTS-Ls with high TargetP scores were identified (Figure S6). Four truncated forms of WWP2 were constructed as per the prediction, with MUT1 expressing proteins harboring deletion of the first potential iMTS-L (located in the C2 domain, between residues 147 and 220), MUT2 expressing proteins harboring deletion of the second potential iMTS-L (located in the WW1 domain, between residues 322 and 389), MUT3 expressing protein harboring deletion of the third potential iMTS-L (located in the WW4 domain, between residues 461 and 529), and MUT1-3 expressing proteins harboring deletion of all three potential iMTS-Ls (Figure 2G). Compared with the full-length WWP2 construct, the four mutants did not influence overall WWP2 expression in mPTCs (Figures 2H and 2I). Deletion of the first and second potential iMTS-Ls did not influence the mitochondrial localization of WWP2 after H/R + T, whereas deletion of the third potential iMTS-L and all three potential iMTS-Ls abrogated the mitochondrial targeting of WWP2 (Figures 2H and 2J). Thus, these results indicated that the mitochondrial targeting of WWP2 is mediated mainly through the sequence located between residues 461 and 529.

WWP2 induced polyubiquitination of the complex II subunit SDHC and mediated TEC mitochondrial dysfunction

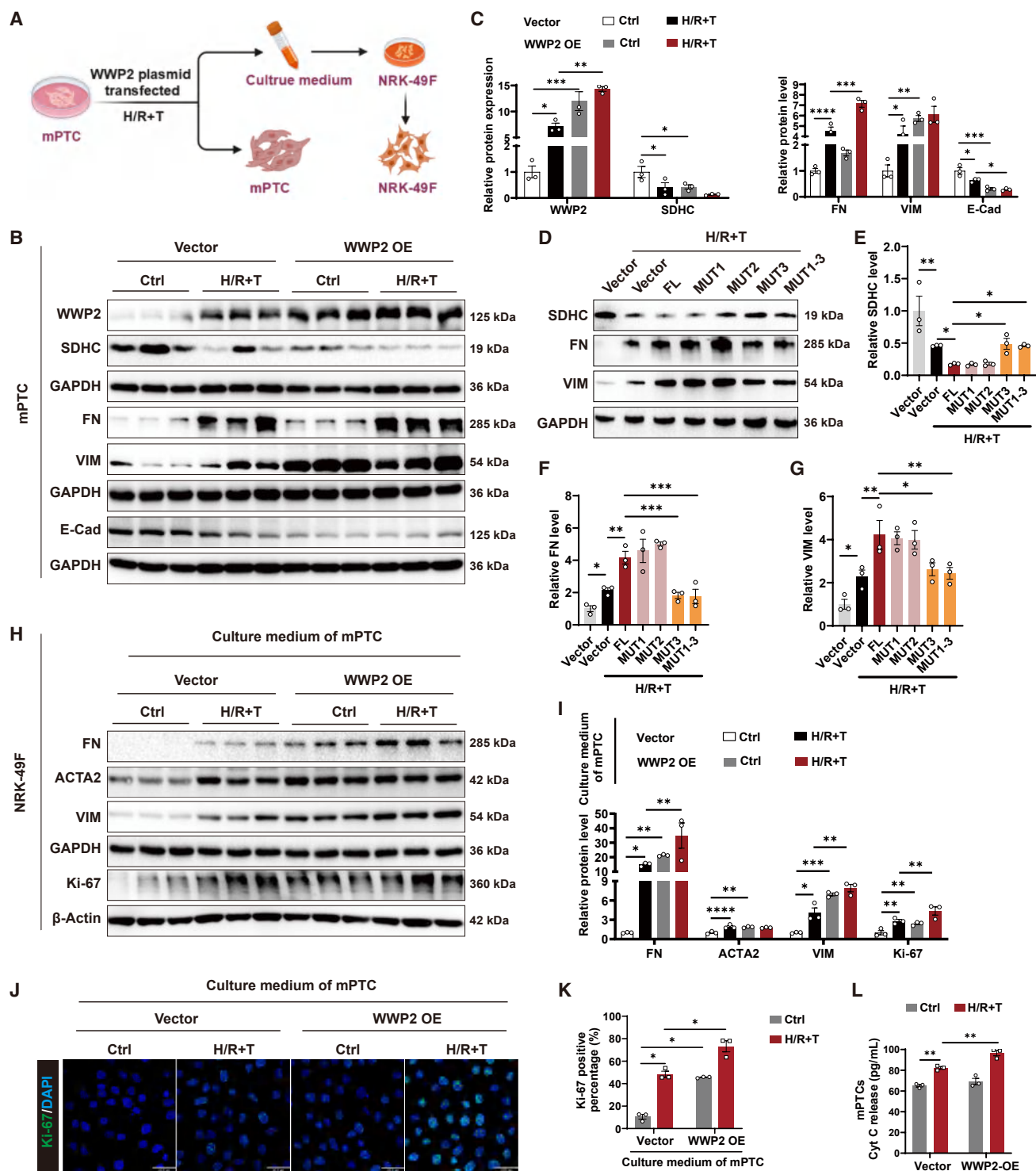
Next, we aimed to determine the main function of WWP2 within mitochondria. As an E3 ubiquitin ligase, WWP2 may regulate mitochondrial function by targeting key mitochondrial proteins for ubiquitination. To identify the possible mitochondrial substrate protein, we overexpressed WWP2 in mPTCs and subjected the cells to ubiquitylation-omics analysis.²³ Focusing on the mitochondrial component, we found that three proteins (SDHC, NDUFA12, and ATP5F1B) were increasingly ubiquitylated upon WWP2 overexpression (Figure 3A). The most highly ubiquitylated mitochondrial protein was SDHC, which was ubiquitylated on lysine within the peptide

NAAPLGTTAKEEMER. The ubiquitylation level was increased 5.171-fold (Figure 3A). Among the three candidate substrate proteins, only SDHC significantly decreased in WWP2-overexpressing mPTCs (Figure 3B). According to the molecular docking data of WWP2 (PDB: 4Y07) and complex II (PDB: 8GS8), WWP2 can interact with the SDHC subunit by forming many hydrophobic interactions and hydrogen bonds (Figure 3C). Co-immunoprecipitation (coIP) analysis was then conducted to confirm the interaction between the two proteins. We first overexpressed FLAG-tagged WWP2 in mPTCs and performed coIP with an anti-FLAG antibody. As shown in Figure 3D, SDHC was readily detected in WWP2-containing coIP complexes. We also overexpressed His-tagged SDHC in mPTCs and performed coIP with an anti-His antibody. Western blotting clearly revealed WWP2 in the SDHC-containing coIP complexes (Figure 3E).

Ubiquitination assays followed by SDHC IP revealed polyubiquitylated SDHC in WWP2-overexpressing mPTCs (Figure 3F), suggesting polyubiquitination regulation of WWP2 on SDHC. Consistent with this result, WWP2 overexpression accelerated the turnover of the SDHC protein (Figure 3G). After treatment with the protein synthesis inhibitor cycloheximide (CHX), the endogenous SDHC gradually degraded, with a half-life above 12 h in the control (Ctrl) cells. In contrast, the half-life of the SDHC decreased to approximately 3 h in the WWP2 OE cells (Figure 3G). Together, these findings suggest that elevated WWP2 level mediates the polyubiquitination and degradation of SDHC in TECs.

Given that SDHC is an important component of complex II, we next focused on whether abnormally high WWP2 expression in TECs led to TCA cycle interruption and OXPHOS disability. As expected, WWP2 overexpression resulted in decreased complex II activity, accumulation of succinate in the culture medium, reduced cellular ATP levels, decreased mitochondrial membrane potential (MMP), and increased mitochondrial ROS (mtROS) within cells (Figures 3H–3L). Seahorse analysis also revealed decreased mitochondrial respiration ability in WWP2 OE mPTCs, with decreased levels of basal respiration and ATP production (Figures 3M and 3N). Under H/R + T challenge, WWP2 OE significantly aggravated the extent of complex II inactivation, succinate accumulation, ATP level reduction, MMP decrease, mtROS bursting, and respiration disability (Figures 3H–3N). Overall, we concluded that during the AKI-to-CKD transition, the increased WWP2 shuttled to the mitochondria, where it targeted the SDHC for polyubiquitylation, promoted its degradation, and mediated TCA cycle interruption and OXPHOS disability in TECs.

WWP2. (F) In-cell ubiquitylation analysis of SDHC in mPTCs transfected with vectors or *Wwp2* overexpression plasmids. The cells were treated with MG132 (10 μ M) for 2 h before being harvested for analysis. (G) mPTCs transfected with vectors or *Wwp2* overexpression plasmids were treated with CHX (10 μ g/mL) and collected at 0, 3, 6, 9, and 12 h. Time-lapse SDHC expression levels were estimated by western blotting. Bars represent quantification results (mean \pm SEM, $n = 3$ independent experiments). (H–L) mPTCs were transfected with *Wwp2* overexpression plasmids and treated with H/R + T. Cells were harvested for the measurement of complex II activity, ATP, MMP, and mtROS levels. The culture medium was collected for the succinate concentration assay. Bars represent quantification results (mean \pm SEM, $n = 3$ or 4 independent experiments). (M) mPTCs were treated as in (H)–(L). A Seahorse mitochondrial stress test was conducted to estimate the oxygen consumption rate (OCR). Bars represent quantification results (mean \pm SEM, $n = 5$ independent experiments for Ctrl and WWP2 OE groups, $n = 12$ for H/R + T group, $n = 10$ for WWP2 OE H/R + T group). (N) Bar plots summarizing the phenotypes derived from the Seahorse mitochondria stress test. An unpaired Student's *t* test was used to assess the statistical significance of differences between two groups for (B) and (G). Two-way ANOVA was used to determine the *p* values for (H)–(L) and (N). **p* < 0.05; ***p* < 0.01; ****p* < 0.001; *****p* < 0.0001.



(legend continued on next page)

Aggravation of TEC maladaptive repair by WWP2 promoted the activation and proliferation of fibroblasts

We then aimed to determine the role of WWP2 in TEC maladaptive repair. Since maladaptive repair of TECs is characterized by an increased secretion phenotype that is closely linked to fibroblast activation,²⁶ we also cultured fibroblasts *in vitro* with conditioned medium from H/R + T-treated mPTCs (Figure 4A). WWP2 overexpression directly mediated SDHC degradation and aggravated H/R + T-induced maladaptive repair of mPTCs, as evidenced by increased expression of the FN and VIM proteins and decreased expression of the epithelial marker protein E-cadherin (E-Cad) (Figures 4B and 4C). Importantly, iMTS-L ablation in WWP2 (MUT3 and MUT1-3) abolished the SDHC regulation and prodedifferentiation ability of WWP2 in H/R + T-induced mPTCs (Figures 4D–4G).

Moreover, we found that the medium from WWP2 OE mPTCs significantly promoted the expression of FN, ACTA2, VIM, and Ki-67 in NRK-49F cells, indicating that the re-arranged metabolism or secreted substances of WWP2 OE mPTCs significantly promoted the activation and proliferation of fibroblasts (Figures 4H–4K). Also, the medium from WWP2 OE mPTCs significantly aggravated the extent of maladaptive repair of mPTC under H/R + T stimuli (Figures 4H–4K). Previously, we found that WWP2 overexpression further increased the accumulation of succinate in the culture medium of H/R + T-injured mPTCs (Figure 3I). In addition, data showed that H/R + T treatment led to an increased release of mitochondrial cytochrome *c* (Cyto C) from mPTCs, which was further increased upon WWP2 overexpression (Figure 4L). Both succinate and Cyto C were reported to play important roles in promoting the activation and proliferation of fibroblast cells.^{27,28} *In vivo*, we found that the mitochondrial membrane integrity was dramatically destroyed in UIR mice and efficiently restored in WWP2 KO mice, as evidenced by the expression level of the outer membrane protein Porin1/2 (Porins) (Figure S7). These results indicate that abnormally high WWP2 expression led to SDHC degradation, and mitochondrial OXPHOS dysfunction in TEC complied with mitochondrial structural instability. The imbalanced mitochondrial homeostatic aggravates the extent of TEC maladaptive repair after injury and subsequently facilitates CKD progression by acting on interstitial fibroblasts.

Replenishing SDHC protected mice from acute ischemia injury-induced CKD

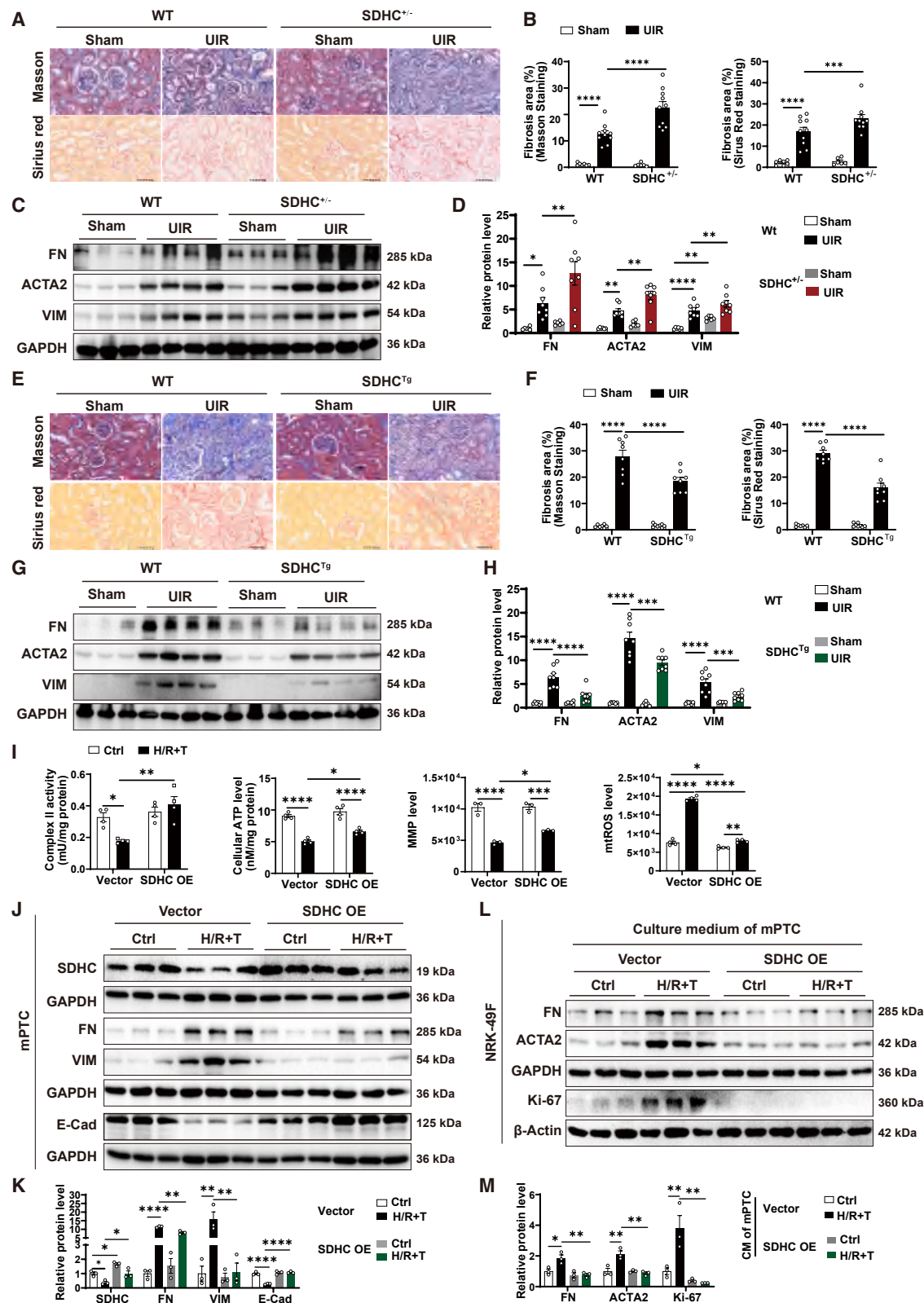
SDHC expression was subsequently estimated in ischemic AKI-to-CKD mice. SDHC expression was downregulated with the progression from AKI to CKD (Figures S8A–S8C). In mPTCs under H/R + T stress, SDHC expression also decreased over time (Figures S8D and S8E).

We first knocked down SDHC to investigate whether it could accelerate ischemia-induced AKI-to-CKD progression. Since *Sdhc* homozygous KO led to death during the embryonic period,²⁹ we generated *Sdhc* heterozygote KO mice (SDHC^{+/-}) by introducing a 62-bp deletion in exon 4 of *Sdhc*. The kidney expression of SDHC in SDHC^{+/-} mice was decreased by 81% (Figures S9A and S9B). SDHC^{+/-} mice bred normally, with body weights matching those of their littermates (Figure S9C). Biochemical analysis did not reveal obvious abnormalities in liver, heart, or kidney function (Figure S9D). Masson and Sirius red staining revealed more aggravated renal lesions and renal fibrosis in the SDHC^{+/-} UIR mice than in the WT UIR mice (Figures 5A and 5B). In line with these findings, FN, ACTA2, and VIM expression levels were higher in the SDHC^{+/-} UIR mice than in the WT UIR mice (Figures 5C and 5D). SDHC knockdown also led to a decreased expression of the other key OXPHOS subunits (Figures S9E and S9F).

We then attempted to replenish the expression of SDHC to investigate whether it could attenuate the AKI-to-CKD transition. *Sdhc* transgenic (SDHC^{Tg}) mice were generated via a hydrodynamic-based tail vein plasmid delivery approach (Figures S10A and S10B), which has been proven to be viable for manipulating gene expression globally.^{30,31} SDHC^{Tg} mice presented body weights (Figure S10C) and serum concentrations of aspartate aminotransferase, creatine kinase-MB, blood urea nitrogen, and serum creatinine similar to those of WT mice (Figure S10D). SDHC^{Tg} and WT mice were subjected to UIR injury. Histological and western blotting analyses revealed attenuated tubule brush border loss and post-UIR renal fibrosis in the SDHC^{Tg} mice compared with that in the WT mice (Figures 5E–5H). Importantly, replenishing SDHC also stabilized the protein levels of the other key subunits of the OXPHOS complexes (Figures S10E and S10F).

In vitro, SDHC overexpression compensated for the H/R + T-induced decrease in complex II activity, the cellular ATP level, and the MMP; furthermore, it eliminated the increase in mtROS levels in mPTCs (Figure 5I). SDHC also significantly attenuated the maladaptive repair of mPTCs, as demonstrated by lower expression of FN and VIM and higher expression of E-Cad in SDHC OE cells (Figures 5J and 5K). Compared with NRK-49Fs treated with conditional medium from H/R + T-treated mPTCs, those treated with conditional medium from H/R + T-injured SDHC-overexpressing mPTCs were protected from abnormal activation and proliferation (Figures 5L and 5M). Taken together, these data suggest that reinforcing SDHC expression could maintain OXPHOS homeostasis and improve the long-term kidney outcome after AKI.

expression plasmids and then subjected to H/R + T. Western blotting was used to detect the expression of SDHC, FN, and VIM. Bars represent quantification results (mean ± SEM, *n* = 3 independent experiments). (H and I) Immunoblots and summary data showing the relative protein levels of FN, ACTA2, VIM, and Ki-67 in NRK-49F cells from different groups. Bars represent quantification results (mean ± SEM, *n* = 3 independent experiments). (J and K) Ki-67 expression levels were evaluated via immunofluorescence staining of NRK-49F cells from different groups. Green, Ki-67; blue, DAPI; scale bar: 36.8 μm. Bars represent quantification results (mean ± SEM, *n* = 3 independent experiments). (L) Cyto C levels were estimated via ELISA in the conditional medium of mPTCs (mean ± SEM, *n* = 3 independent experiments). Two-way ANOVA was used to determine the *p* values for (C), (I), (K), and (L). One-way ANOVA was used to assess the statistical significance of differences between groups for (E)–(G). **p* < 0.05; ***p* < 0.01; ****p* < 0.001; *****p* < 0.0001.



(legend on next page)

WWP2 promoted the AKI-to-CKD transition via the negative regulation of SDHC

To test whether WWP2 promoted the AKI-to-CKD transition via the negative regulation of SDHC, we transfected the *Wwp2* overexpression plasmids and *Sdhc* overexpression plasmids into mPTCs together and exposed the cells to H/R + T stimuli. WWP2 overexpression further disrupted complex II activity, decreased the cellular ATP level, decreased the MMP, and increased the mtROS level in mPTCs after H/R + T stimulation, whereas SDHC overexpression together with WWP2 overexpression reversed these disorders (Figures 6A–6D). SDHC OE compensated for WWP2 OE-induced repression of mitochondrial respiration under H/R + T stimulation (Figure 6E). In parallel, SDHC OE reversed abnormal FN, ACTA2, VIM, and E-Cad expression upon WWP2 OE in H/R + T-treated mPTCs (Figures 6F and 6G). SDHC overexpression also reduced the fibroblast activation ability of injured mPTCs overexpressing WWP2 (Figures 6H and 6I).

We also knocked down SDHC in WWP2 KO mice via hydrodynamic-based tail vein plasmid delivery of the *Sdhc*-targeted CRISPR-Cas9 plasmids and constructed the UIR model thereafter. WWP2 KO mice presented mitigated tubular injury; less extracellular matrix disposition in the tubulointerstitial compartment; lower expression of FN, ACTA2, and VIM; and higher expression of E-Cad—all of which were significantly abolished by SDHC knock-down (Figures 6J–6M). Together, the *in vivo* and *in vitro* data demonstrate that WWP2 promotes the AKI-to-CKD transition via the negative regulation of SDHC.

Restraining WWP2 activity is a potential therapeutic avenue for preventing the AKI-to-CKD transition

The data described above led us to investigate the therapeutic potential of targeting WWP2 to retard the AKI-to-CKD transition. Next, we sought small molecules with WWP2 inhibitory activity and binding affinity to further verify the role of WWP2 in the AKI-to-CKD transition and offer translational potential in the clinic. A virtual molecular docking screening strategy was adopted for screening, and 11 molecules with high docking scores were identified (Figures 7A and 7B). A cell-free WWP2 ubiquitin activity assay was subsequently

performed, and the results revealed that 3 out of the 11 molecules significantly inhibited WWP2 activity (Figure 7C). Cell viability assays were performed to determine the safe concentrations of compound 7 (H9-D10), compound 9 (1-(1-methyl-4-nitro-1H-imidazol-5-yl)-4-piperidinecarboxamide, H36-E4), and compound 11 (1-[5-[(4-chlorobenzyl)thio]-4-nitro-2-thienyl]ethan-1-one, H111-H7) for mPTCs (Figure S11). At safe concentrations, compounds H36-E4 and H111-H7 markedly downregulated the expression of WWP2 and protected mPTCs against TGF- β 1 and H/R + T injury (Figures 7D–7G). The binding affinities of the two molecules were quantified via biolayer interferometry (BLI). The results revealed reliable binding activity between the two molecules and the recombinant human WWP2 protein (Figures 7H–7J). The equilibrium dissociation constant (K_D value) between H36-E4 and WWP2 was 6.25 μ M (Figure 7I), and the calculated K_D value between H111-H7 and WWP2 was 717 nM (Figure 7J). To further illustrate the binding mode for H36-E4 and H111-H7, two-dimensional (2D) and three-dimensional (3D) docking models of the WWP2–H36-E4 and WWP2–H111-H7 complexes were obtained. The docking results revealed that H36-E4 could form stable interactions with favorable residues, including Gln590, Thr627, and Arg633, in the binding pocket of WWP2 (Figure 7K) and that H111-H7 could interact with Thr627 and Arg712 as favorable residues of WWP2 (Figure 7L).

The translational potential of the two identified small molecular WWP2 inhibitors was then evaluated in AKI-to-CKD model mice. The mice received the corresponding drug treatment 72 h after UIR injury. After 18 consecutive days of treatment, kidney fibrotic deposition and Col1A1 expression was significantly decreased in H36-E4 treated UIR mice (Figures 8A–8D). Moreover, the increase in WWP2 expression and the decrease in SDHC expression in UIR mice were markedly mitigated by H36-E4 treatment (Figures 8E and 8F). Western blotting revealed that H36-E4 significantly decreased the extent of tubular maladaptive repair and partially restored the expression of other key OXPHOS subunits (Figures 8E, 8F, S12A, and S12B). H111-H7-treated mice also showed a recovered phenotype with a lower degree of fibrotic deposition, lower WWP2 expression, recovered SDHC protein levels, alleviated tubular maladaptive repair

Figure 5. SDHC overexpression protected OXPHOS function and retarded the AKI-to-CKD transition

(A and B) WT and SDHC^{+/−} mice were subjected to UIR surgery. Representative Masson's trichrome and Sirius red staining images and quantification of the fibrosis area. Scale bar, 50 μ m. Bars represent quantification results (mean \pm SEM, n = 7 mice for WT sham group, n = 6 mice for SDHC^{+/−} sham group, and n = 10 mice for WT UIR and SDHC^{+/−} UIR groups). (C and D) Representative immunoblots and associated densitometry analyses of FN, ACTA2, and VIM in whole-kidney protein lysates from different groups. Bars represent quantification results (mean \pm SEM, n = 6 mice for WT sham and SDHC^{+/−} sham groups, and n = 8 mice for WT UIR and SDHC^{+/−} UIR groups). (E and F) SDHC^{T9} mice were subjected to UIR modeling. Representative Masson's trichrome and Sirius red staining images and quantification of the fibrosis area are shown. Scale bar, 50 μ m. Bars represent quantification results (mean \pm SEM, n = 7 mice for WT sham group, and n = 8 mice for WT UIR, SDHC^{T9} sham, and SDHC^{T9} UIR groups). (G and H) Representative western blot images and summary data showing the relative protein levels of FN, ACTA2, and VIM in different groups of mice. Bars represent quantification results (mean \pm SEM, n = 6 mice for WT sham and SDHC^{T9} sham groups, and n = 8 mice for WT UIR and SDHC^{T9} UIR groups). (I) mPTCs were transfected with *Sdhc* overexpression plasmids and treated with H/R + T. Complex II activity (n = 4), the cellular ATP level (n = 4), the MMP level (n = 3), and the mtROS level (n = 4) in each group were measured. Bars represent quantification results (mean \pm SEM). (J and K) mPTCs overexpressing SDHC were harvested after H/R + T stimulation. Immunoblots and summary data showing the relative protein levels of SDHC, FN, VIM, and E-Cad in mPTCs from different groups. Bars represent quantification results (mean \pm SEM, n = 3 independent experiments). (L and M) The conditioned medium from mPTCs of (J) and (K) was collected and added to NRK-49Fs. NRK-49Fs were collected for analysis after 24 h of treatment. Representative immunoblots and quantification data of FN, ACTA2, and Ki-67 expressions are shown. Bars represent quantification results (mean \pm SEM, n = 3 independent experiments). Two-way ANOVA was used to determine the p values for (B), (D), (F), (H), (I), (K), and (M). * p < 0.05; ** p < 0.01; *** p < 0.001; **** p < 0.0001.

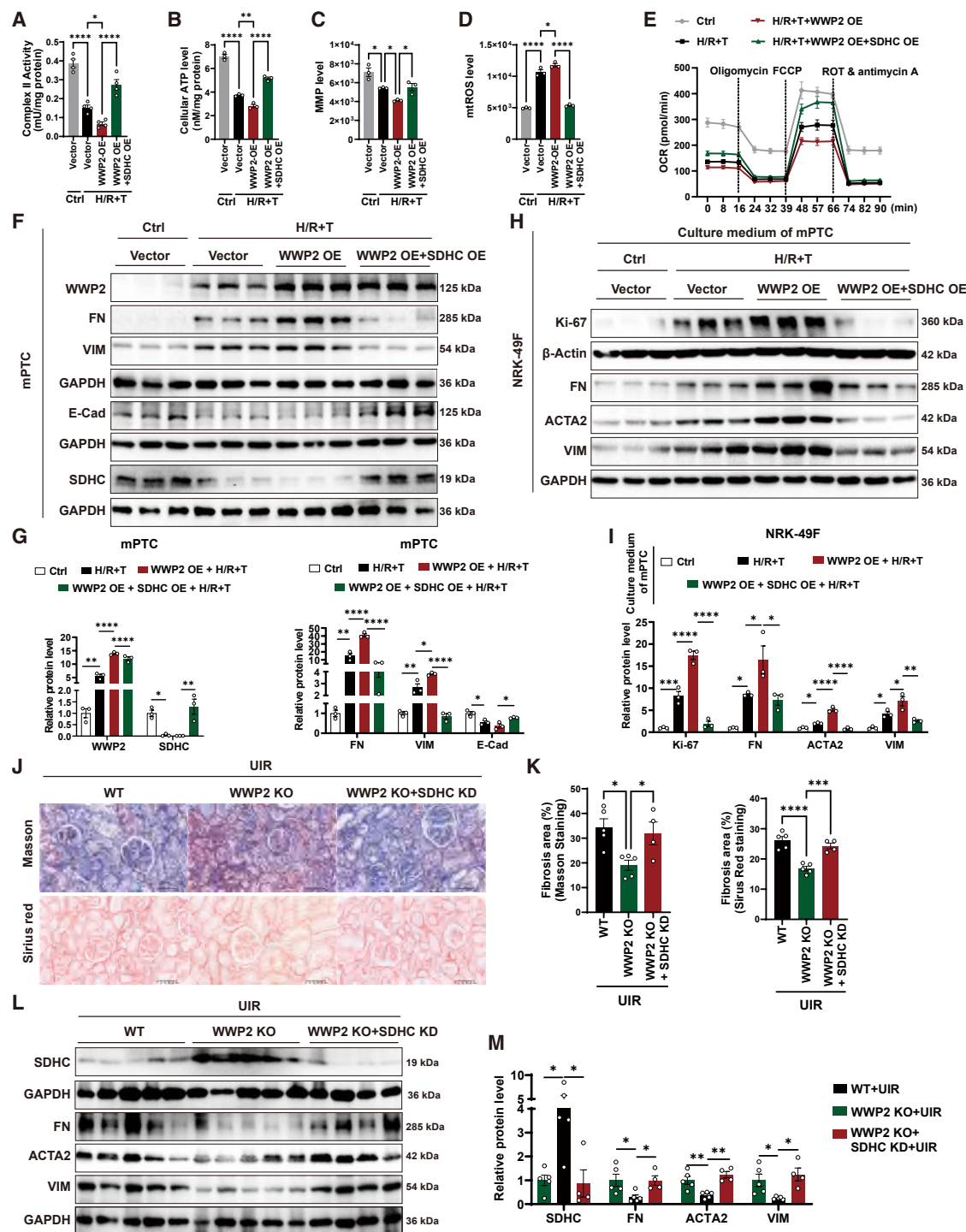


Figure 6. SDHC is involved in WWP2-mediated TEC OXPHOS dysfunction and the AKI-to-CKD transition

(A–D) mPTCs were co-transfected with *Wwp2* and *Sdhc* overexpression plasmids and stimulated with H/R + T. Complex II activity ($n = 4$), the cellular ATP level ($n = 3$), the MMP level ($n = 3$), and the mtROS level ($n = 3$) in each group were measured. Bars represent quantification results (mean \pm SEM). (E) mPTCs were treated as described in (A)–(D). A Seahorse mitochondrial stress test was conducted to estimate the mitochondrial respiration ability in each group. Bars represent quantification results (mean \pm SEM, $n = 5$ for Ctrl group, $n = 12$ for H/R + T, H/R + T + WWP2 OE, and H/R + T + WWP2 OE + SDHC OE groups). (F and G) mPTCs were treated as described in (A)–(D). Immunoblots and quantification of WWP2, SDHC, FN, VIM, and E-Cad expression in different groups are shown. Bars represent quantification results (mean \pm SEM, $n = 3$

(legend continued on next page)

and partially restored expression of other OXPHOS subunits on day 21 after UIR (Figures 8G–8L, S12C, and S12D).

Moreover, the potential toxicity of H36-E4 and H111-H7 were assessed. The results showed that treatment with therapeutic doses of H36-E4 and H111-H7 for 18 consecutive days did not affect body weight or serum indices of renal, liver, or heart function (Figures S13A–S13G). In renal tissue, H36-E4 and H111-H7 did not increase the expression of kidney injury marker neutrophil gelatinase-associated lipocalin (NGAL) (Figures S13H and S13I) and transcription level of key inflammatory factors (*Tnf* and *Il1b*) (Figures S13J–S13K). These findings demonstrate that restraining WWP2 activity might represent a promising strategy for attenuating the AKI-to-CKD transition.

DISCUSSION

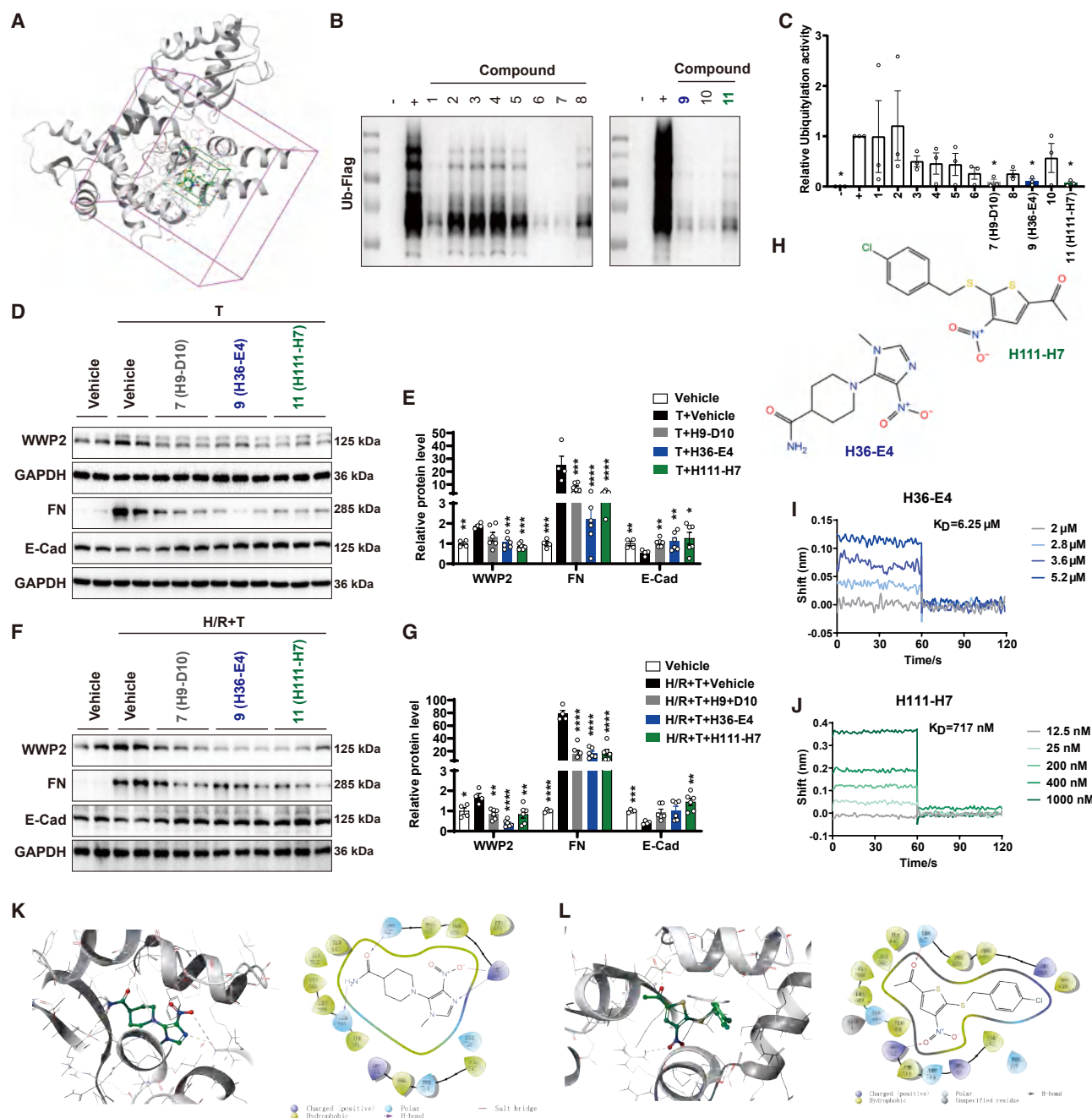
Energy supply is particularly important for the kidney because it is an important metabolic organ that requires a high energy supply to maintain its basic function in regulating hemodynamics, maintaining acid-base and electrolyte balance, reabsorbing nutrients, and secreting hormones.³² TECs, which are highly metabolically active and rely on FAO coupled with OXPHOS and the TCA cycle for ATP generation, are the primary site of damage during AKI. Among the five multisubunit OXPHOS complexes (I–V), complex II is the only enzyme complex involved both in the TCA cycle and OXPHOS. Specifically, the SDHA and SDHB subunits form the main catalytic domain that mediates the oxidation of succinate to fumarate in the TCA cycle, and the membrane-anchored SDHC and SDHD subunits play a role in transferring electrons to complex III.³³ Research has demonstrated that OXPHOS dysfunction is involved in the pathological conditions of AKI and CKD.^{10,34–36} Additionally, we verified for the first time that restoring SDHC expression could maintain mitochondrial OXPHOS stability and decelerate the AKI-to-CKD progression and vice versa. However, the prime culprit that directly mediates OXPHOS dysfunction has long been unresolved.

Interestingly, time-lapse subcellular localization analysis and immunofluorescent analysis revealed that WWP2 tended to translocate to the mitochondria during the AKI-to-CKD transition. Unbiased transcriptional analysis revealed that proximal tubular *Wwp2* ablation predominantly re-established the disturbed OXPHOS pathway. Ubiquitylation-omics analysis of WWP2-overexpressing mPTCs revealed three possible mitochondrial substrate proteins of WWP2, among which SDHC expression was significantly downregulated upon WWP2 overexpression. Molecular docking, coIP analysis, an

SDHC ubiquitylation assay, and protein stability evaluation were further conducted, and the results verified the interaction between WWP2 and SDHC proteins, with the former promoting the polyubiquitination and subsequent degradation of SDHC. We also identified that the mitochondrial targeting of WWP2 is mediated through the iMTS-L located between residues 461 and 529. According to the multiways of protein translocation summarized by Busch et al.,³⁷ WWP2 may be translocated across the outer membrane through the translocase of the outer mitochondrial membrane complex and then guided through the intermembrane space by translocase of the inner membrane. Thus, our research indicates for the first time that the E3 ubiquitin ligase WWP2 enters mitochondria and mediates OXPHOS dysfunction by promoting the polyubiquitination of the complex II subunit SDHC during the AKI-to-CKD transition. Further studies are needed to affirm the detailed mitochondrial transportation mechanism and mitochondrial localization (intermembrane space, inner membrane, or matrix) of WWP2.

This finding provides a potential strategy for maintaining OXPHOS stability under stress—that is, protecting SDHC from WWP2-mediated polyubiquitination. With this intent, we aimed to screen potential WWP2 inhibitors. Since WWP2 has been reported to drive cancer tumorigenesis and metastasis,^{17,18} researchers have previously identified small-molecule WWP2 inhibitors for antitumor purposes.³⁸ However, the screening library is relatively small (2,043 molecules in total). In our study, we screened over 14,400 molecules in the Maybridge HitFinder library using high-throughput computer-based virtual screening. The WWP2-inhibiting effects of the candidate molecules with high scores were tested via a ubiquitination assay in a cell-free system, and the protective effects of the candidate molecules were further evaluated in TGF- β 1- and H/R + T-injured mPTCs. After the above-mentioned three rounds of screening, compounds H36-E4 and H111-H7 were selected as hit compounds. A BLI assay further confirmed the binding of the two hits with the recombinant WWP2 protein. Notably, compounds H36-E4 and H111-H7, which were administered after the acute injury phase, both robustly inhibited the expression of WWP2, restored the SDHC level, and alleviated the AKI-to-CKD transition in an acute ischemia-induced AKI-to-CKD mouse model. Moreover, the two molecules also partially restored the expression of other key OXPHOS subunits due to the secondary effect of restored SDHC expression. Thus, this research identified two WWP2 inhibitors for further development in AKI-to-CKD-retarding therapeutics. In addition to mediating the AKI-to-CKD transition, WWP2 has been reported to mediate tumor progression,^{17,18} cardiac

independent experiments). (H and I) NRK-49Fs were treated with conditional medium from the mPTCs in (F). Immunoblots and quantification of Ki-67, FN, ACTA2, and VIM expressions in different groups are shown. Bars represent quantification results (mean \pm SEM, $n = 3$ independent experiments). (J and K) WWP2 KO mice were injected with *Sdhc*-targeted CRISPR-Cas9 plasmids for *Sdhc* knockdown (SDHC KD) via a hydrodynamic-based tail vein plasmid delivery approach and subjected to UIR modeling. Kidney fibrosis levels were estimated via Masson's trichrome and Sirius red staining. Quantification of the fibrosis area is shown in parallel. Scale bar, 50 μ m. Bars represent quantification results (mean \pm SEM, $n = 5$ mice for WT UIR and WWP2 KO UIR groups, and $n = 4$ mice for the WWP2 KO + SDHC KD UIR group). (L and M) Representative western blot images and summary data showing the relative protein levels of SDHC, FN, ACTA2, and VIM in different groups of mice. Bars represent quantification results (mean \pm SEM, $n = 5$ mice for WT UIR and WWP2 KO UIR groups, and $n = 4$ mice for the WWP2 KO + SDHC KD UIR group). One-way ANOVA was used to assess the statistical significance of differences between groups for (A)–(D), (G), (I), (K), and (M). * $p < 0.05$; ** $p < 0.01$; *** $p < 0.001$; **** $p < 0.0001$.



(legend continued on next page)

hypertrophy, and fibrosis.^{19,20} Thus, these two WWP2 inhibitors may also be therapeutic candidates for these diseases.

Notably, our team previously reported that WWP2 protects against cisplatin induced acute tubular epithelial cell injury and renal dysfunction by targeting the polyubiquitination of CDC20, thus promoting autophagy.²³ Additionally, our cooperative team recently reported the pathogenic role of WWP2 in mediating myofibroblast proliferation and profibrotic activation during renal fibrosis via transcriptional suppression of peroxisome proliferator-activated receptor gamma coactivator 1- α (PGC-1 α).³⁰ In contrast to these two studies, the present study elucidated the pathological role of WWP2 in mediating TEC maladaptive repair and the AKI-to-CKD transition. By constructing WWP2 iKO mice and initiating *Wwp2* depletion before and after the acute phase of AKI, we found that *Wwp2* ablation, whether initiated before or after AKI, eventually resulted in reduced tubular injury and tubulointerstitial fibrosis. In summary, we conclude that during AKI, WWP2 predominantly acts on CDC20 and promotes autophagy to limit tubular epithelial injury. However, if the injury is unrepairable, then WWP2 shuttles to the mitochondria and targets SDHC for polyubiquitination and degradation, leading to OXPHOS dysfunction and maladaptive repair of TECs, thus promoting the AKI-to-CKD transition. In the later phase of CKD, when myofibroblasts play a dominant role in mediating kidney fibrosis, WWP2 suppresses the transcription of PGC-1 α in myofibroblasts and leads to metabolic reprogramming and profibrotic activation of this group of cells. Thus, although statistics showed that whole-course WWP2 inhibition restrained AKI-to-CKD progression, we suggest that WWP2 inhibition be initiated after the acute phase of AKI to avoid unnecessary tubular deterioration.

Our study provides evidence that injured TECs with high-level WWP2 expression also promote the activation and proliferation of renal tubulointerstitial fibroblast cells. Our data showed that H/R + T treatment led to an increased accumulation of succinate and release of Cyto C in the culture medium of mPTECs, and WWP2 overexpression further increased the levels. Previously, various studies have shown that the accumulation of succinate has the potential to enhance inflammatory signaling in activated macrophages by acting on succinate receptor 1.^{39,40} Recently, it was also reported that succinate treatment increased the expression of fibrosis-associated markers and exaggerated TGF- β -mediated fibroblast-to-myofibroblast transition in human lung fibroblasts.²⁸ Thus, succinate accumulation may stimulate the activation and proliferation of renal tubulointerstitial fibroblast cells both directly and indirectly (via macrophage-fibroblast crosstalk). The release of Cyto C from mitochondria into the cytosol is a well-established key step in initiating apoptosis. Upon cell necrosis or apoptosis,

Cyto C is released into the interstitial space and circulation. Recent studies indicate that extracellular Cyto C can function as a damage-associated molecular pattern (DAMP) molecule.⁴¹ By activating DAMP receptors, Cyto C is reported to alter cellular functions such as proliferation, migration, myofibroblast transdifferentiation, extracellular matrix turnover, and the production of fibrotic and inflammatory paracrine factors in cardiac fibroblasts.²⁷ Importantly, Cyto C leakage means the release of various other molecules that serve as DAMPs, such as mtDNA, cardiolipin, and N-formyl peptides. These mtDAMPs could initiate sterile inflammation via numerous signaling pathways. Thus, the release of Cyto C and other mtDAMPs from epithelial cells may also play an important role in mediating the activation and proliferation of renal tubulointerstitial fibroblast cells.

This study has two main limitations. First, the clinical sample number in this study is relatively small. The collection of renal tissue samples from clinical patients with AKI-to-CKD progression is challenging due to the extended progression period of AKI-to-CKD transition, and patients often receive diagnosis and treatment across multiple medical centers at different disease stages. Thus, this study only included renal tissue specimens from four pediatric CKD patients with a clear history of AKI, along with four samples of adjacent normal renal tissue obtained after renal cancer resection, which served as the normal control group. A multicenter study will be conducted in the later phase of this research to further expand the clinical sample size. Second, this study primarily focuses on the role and mechanism of WWP2 in renal tubular epithelial cells during AKI-to-CKD progression. Further research is warranted to elucidate the regulatory role of WWP2 in other types of cells and its influence on the outcomes of AKI-to-CKD transition.

In conclusion, in response to AKI, WWP2 is increasingly expressed and translocated to mitochondria, where it acts on the complex II core subunit SDHC, facilitating SDHC polyubiquitination and degradation. WWP2-mediated degradation of SDHC disrupted the TCA cycle and the integrity of mitochondrial OXPHOS, mediated the maladaptive repair of TECs, and promoted the AKI-to-CKD transition. The development of genetic and pharmacological approaches for WWP2 inhibition could be an effective strategy to restore OXPHOS and prevent the AKI-to-CKD transition in the clinic (Figure 8M).

MATERIALS AND METHODS

Kidney biopsy evaluation in humans

Normal human renal tissues were nondiseased portions of the kidney from renal cell carcinoma patients who underwent tumor-removal surgery. Injured human kidney samples were obtained from CKD patients with a clear history of AKI (without other primary or secondary kidney diseases, such as immune-related kidney

T + vehicle group). (H) Chemical structures of H36-E4 and H111-H7. (I) A biolayer interferometry (BLI) system was used to estimate the physical interaction between H36-E4 and the recombinant WWP2 protein. (J) A BLI system was used to estimate the physical interaction between H111-H7 and the recombinant WWP2 protein. (K) Proposed binding model of H36-E4 to the human WWP2 HECT domain (PDB: 4Y07). Three- and two-dimensional illustrations are shown. (L) Proposed binding model of H111-H7 to the human WWP2 HECT domain (PDB: 4Y07). Three- and two-dimensional illustrations are shown. * $p < 0.05$; ** $p < 0.01$; *** $p < 0.001$; **** $p < 0.0001$.



(A–D) Mice were subjected to UIR and treated with the candidate WWP2 inhibitor H36-E4 (4 mg/kg) 3 days after UIR injury. The mice were euthanized after 18 continuous days of treatment. Kidney fibrosis was determined by Masson's trichrome staining, Sirius red staining, and immunohistochemical staining of Col1A1. Scale bar, 50 μ m. Bars represent quantification results (mean \pm SEM, n = 6 mice for vehicle sham group, n = 8 mice for vehicle UIR group, and n = 9 mice for H36-E4 sham and H36-E4 UIR groups).

diseases, diabetic nephropathy, hypertensive nephropathy, etc.) The protocol for using renal samples from patients was approved by the local committee on human subjects at the Children's Hospital of Nanjing Medical University (Nanjing, China). All participants provided written informed consent.

Mouse strains

WWP2^{fl/fl} mice and proximal tubule conditional Wwp2 KO (WWP2 PT^{CKO}) mice on a C57BL/6J background were generated in our laboratory as described previously.²³ WWP2 iKO mice were generated by crossbreeding WWP2^{fl/fl} mice with CAG-CreERT2 mice (stock no. 004682, The Jackson Laboratory, Bar Harbor, ME). The WWP2 iKO mice were injected with tamoxifen (20 mg/mL/day) (HY-13757A, MCE, Monmouth Junction, NJ) for 5 consecutive days to initiate Wwp2 gene depletion. SDHC^{+/-} mice, generated via the CRISPR-Cas9 system, were purchased from GemPharmatech (strain no. T062141, Nanjing, China). SDHC^{Tg} mice were generated by administering the *Sdhc* overexpression plasmid to C57BL/6J mice via a hydrodynamic-based tail vein plasmid delivery approach, which was previously demonstrated to be viable for manipulating gene expression globally.^{30,31} All the mice were bred and maintained in a specific pathogen-free room with free access to water and food, an automatic 12-h light/dark cycle, a constant temperature (22°C ± 2°C), and a relative air humidity of approximately 50%.

Mouse modeling and treatment

UIR-induced AKI-to-CKD progression mouse models were generated as previously described.³¹ Briefly, UIR modeling was established by clamping the right renal pedicles of the mice for 35 or 45 min and then releasing them to allow reperfusion. The mice were sacrificed on days 1, 3, 10, 21, or 28 after UIR, as indicated in each experiment. To establish the repeated-CP model, mice received weekly injections of 10 mg/kg CP (catalog no. 232120, Sigma-Aldrich, St. Louis, MO) or the same volume of saline for 4 weeks and were sacrificed 7 days after the last injection.^{42,43} To investigate the impact of two candidate WWP2 inhibitors on the AKI-to-CKD transition, we subjected C57BL/6J mice (8 weeks old, male, purchased from GemPharmatech) to UIR modeling. Three days after UIR injury, the mice received daily intraperitoneal injections of H36-E4 (CAS:

688310-17-0) (4 mg/kg) (>99%, catalog no. HTS03118, Maybridge/Thermo Fisher Scientific, Waltham, MA) or H111-H7 (CAS: 220965-54-8) (1 mg/kg) (>98%, catalog no. KM03206, Maybridge/Thermo Fisher Scientific). The mice were sacrificed after 18 days of treatment. All the animal experiments were performed at the Animal Core Facility of Nanjing Medical University, and all the procedures were approved by the Nanjing Medical University Institutional Animal Care and Use Committee.

Kidney histological examination

Kidney sections were fixed with 4% paraformaldehyde (PFA) and then embedded in paraffin. Masson's trichrome staining and Sirius red staining were conducted on deparaffinized tissues using commercial kits (catalog no. g1006, ServiceBio, Wuhan, China; catalog no. RS1240, G-Clone, Beijing, China) as per the manufacturer's instructions.

Immunofluorescence analysis

The kidney sections were deparaffinized, rehydrated, heated in citrate buffer, and blocked with 5% normal goat serum. mPTCs were cultured in glass-bottom cell culture dishes, treated as indicated, fixed with 4% PFA, and permeabilized with 0.1% Triton X-100/PBS. Then, the cells and tissue slides were blocked with 2% BSA/PBS for 1 h and incubated with primary antibodies overnight at 4°C. The following fluorescein agents and primary antibodies were used: fluorescein-conjugated *Lotus tetragonolobus* lectin (1:50, FL-1321-2, Vector Laboratories, Newark, CA), WWP2 (1:200, catalog no. 12197-1-AP, ProteinTech, Rosemont, IL), TOMM20 (1:50, catalog no. ab56783, Abcam, Cambridge, MA), SDHC (1:200, catalog no. A21040, Abclonal, Wuhan, China), and Ki-67 (1:400, catalog no. 9129, Cell Signaling Technology, Danvers, MA). The secondary antibodies (1:1,000, Alexa Fluor 488-conjugated goat anti-rabbit immunoglobulin G [IgG], catalog no. ab150077, Abcam; 1:1,000, Alexa Fluor 555-conjugated goat anti-mouse IgG, catalog no. 150114, Abcam; 1:300, Alexa Fluor 555-conjugated donkey anti-rabbit IgG, catalog no. A0453, Beyotime, Shanghai, China) were incubated for 2 h, followed by DAPI staining (catalog no. C1006, Beyotime) for 15 min. The slides were observed and photographed with a Leica STELLARIS 5 confocal microscope (Leica Microsystems, Wetzlar, Germany) or an Olympus BX51 microscope (Olympus, Tokyo, Japan).

(E and F) Representative western blot images and summarized data showing the relative protein levels of WWP2, SDHC, FN, and ACTA2 in different groups of mice. Bars represent quantification results (mean ± SEM, *n* = 6 mice for vehicle sham and H36-E4 sham groups, *n* = 8 mice for vehicle UIR and H36-E4 UIR groups). (G–J) Mice were subjected to UIR and treated with the candidate WWP2 inhibitor H111-H7 (1 mg/kg) 3 days after UIR injury. The mice were euthanized after 18 continuous days of treatment. Kidney fibrosis was determined by Masson's trichrome staining, Sirius red staining, and immunohistochemical staining of Col1A1. Scale bar, 50 μm. Bars represent quantification results (mean ± SEM, *n* = 6 mice for vehicle sham group, *n* = 8 mice for vehicle UIR group, and *n* = 9 mice for H111-H7 sham and H111-H7 UIR groups). (K and L) Representative immunoblots and quantitative data showing the relative protein levels of WWP2, SDHC, FN, and ACTA2 in mouse kidneys. Bars represent quantification results (mean ± SEM, *n* = 6 mice for vehicle sham and H111-H7 sham groups, and *n* = 8 mice for vehicle UIR and H111-H7 UIR groups). Two-way ANOVA was used to determine the *p* values for (B)–(D), (F), (H)–(J), and (L). **p* < 0.05; ***p* < 0.01; ****p* < 0.001; *****p* < 0.0001. (M) Schematic illustration of the role of WWP2 in the AKI-to-CKD transition. In response to severe AKI, WWP2 is increasingly expressed and shuttled to mitochondria in TECs. Mitochondrial WWP2 targeted the complex II core subunit SDHC for polyubiquitination and degradation. Extensive degradation of SDHC disrupted the TCA cycle and the integrity of mitochondrial OXPHOS, mediated the maladaptive repair of TECs, and promoted the AKI-to-CKD transition. Two candidate molecules, H36-E4 and H111-H7, which possess WWP2 inhibitory ability and binding affinity, significantly deferred the AKI-to-CKD transition. ADP, adenosine diphosphate; ATP, adenosine triphosphate; CoQ, coenzyme Q; Cyto C, cytochrome c; ETC, electron transportation chain; H36-E4, 1-[1-methyl-4-nitro-1H-imidazol-5-yl]-4-piperidinecarboxamide; H111-H7, 1-[5-[[4-chlorobenzyl]thio]-4-nitro-2-thienyl]ethan-1-one; IMM, inner mitochondrial membrane; IR, ischemia-reperfusion; MM, mitochondrial matrix; OMM, outer mitochondrial membrane; TCA cycle, tricarboxylic acid cycle.

Immunohistochemical staining

Kidney tissues were fixed in 4% PFA, embedded in paraffin, and cut at a thickness of 3 μ m. After deparaffinization via xylene and graded ethanol, the tissue slides were microwaved in citrate antigen repair solution (catalog no. P0083, Beyotime) for antigen repair and incubated in 3% hydrogen peroxide for 20 min. The tissue slides were then blocked and incubated overnight at 4°C with anti-WWP2 (1:100, catalog no. 12197-1-AP, ProteinTech) or anti-Col1A1 (1:200, catalog no. 72026, Cell Signaling Technology) antibodies. After being washed with PBS with Tween 20, the tissue slides were incubated with horseradish peroxidase (HRP). The localization of peroxidase conjugates was eventually determined with a commercial 3,3'-diaminobenzidine kit (catalog no. PV-9000, ZSBO, Beijing, China). Nuclei were stained with hematoxylin. The signals were detected via a pathological slice scanner (catalog no. KF-PRO-020, Kfbio, Ningbo, China), and the intensity of the positively stained area was quantified with Image-Pro Plus software (Media Cybernetics, Rockville, MD).

Cell culture, transfection, and treatment

mPTCs and NRK-49F cells were obtained from the American Type Culture Collection (Manassas, VA). The mPTCs were cultured in DMEM/F12 medium (catalog no. C11330500BT, Gibco, Thermo Fisher Scientific, Halethorpe, MD); the NRK-49Fs were cultured in DMEM (catalog no. C11995500BT, Gibco) supplemented with 10% fetal bovine serum (catalog no. 10099-141C, Gibco), penicillin (100 U/mL), and streptomycin (100 μ g/mL) in a humidified 37°C incubator supplemented with 5% CO₂. The overexpression of WWP2 or SDHC in mPTCs was achieved via the transfection of a FLAG-tagged *Wwp2* plasmid or a His-tagged *Sdhc* plasmid with PolyJet In Vitro DNA Transfection Reagent (catalog no. SL100688; SignaGen Laboratories, Frederick, MD). For SDHC knockdown, mPTCs were transfected with small interfering RNAs targeting mouse *Sdhc* (catalog nos. siG2104220202586904, siG2104220202587996, and siG2104220202589088, RiboBio, Guangzhou, China) using Lipofectamine 2000 transfection reagent (catalog no. 11668500, Thermo Fisher Scientific). For H/R + T stimuli, to mimic AKI-to-CKD pathological conditions *in vitro*, mPTCs or NRK-49F cells were cultured in a hypoxia condition (1% O₂) for 12 h, followed by reoxygenation and TGF- β 1 (5 μ g/mL) treatment for another 24 h before being harvested for further analysis. For CoCl₂ + T stimuli, mPTCs were treated with CoCl₂ (200 nM) for 12 h to induce chemical hypoxia, followed by washouts and TGF- β 1 (5 μ g/mL) treatment for another 24 h before being harvested for further analysis. H36-E4 (1 μ M) and H111-H7 (0.25 μ M) were applied at the time of reoxygenation. In cellular cross-talk experiments, NRK-49F cells were treated with the conditioned medium of mPTCs for 24 h.

Nucleus, mitochondrial, and cytosolic components separation

According to the instructions of the Invent Biotechnologies (Eden Prairie, MN) mitochondria isolation kit (catalog no. MP-007), cells ($>40 \times 10^6$) or tissues (20–30 mg) were lysed in 250 μ L buffer A on ice. All samples underwent centrifugation at $16,000 \times g$ for 30 s. Nucleus pellets were resuspended in protein lysis buffer, while

supernatants were transferred to new tubes, mixed with 300 μ L buffer B, and centrifuged at $16,000 \times g$ for 30 min to obtain cytosolic/membrane proteins in supernatants. For mitochondrial isolation, pellets were resuspended in 200 μ L buffer B, centrifuged at $8,000 \times g$ for 5 min, and the supernatants were re-centrifuged at $16,000 \times g$ for 15 min after mixing with 1.6 mL PBS. The purified mitochondrial pellets were obtained and resuspended in lysis buffer.

Truncated mutants of *Wwp2*

The TargetP algorithm was used to predict the iMTS-Ls within the mouse WWP2 protein.^{24,25} Sequences with high TargetP scores were selected and truncated, resulting in the following truncated sequences: MUT1 expressing proteins harbored deletion of residues between 147 and 220, MUT2 expressing proteins harbored deletion of residues between 322 and 389, MUT3 expressing proteins harbored deletion of residues between 461 and 529, and MUT1-3 expressing proteins harbored deletion of all three potential iMTS-Ls (Figure 2G). These four truncated sequences were then inserted into the eukaryotic expression vector pcDNA3.1 to construct *Wwp2* mutant plasmids.

SDHC protein stability

mPTCs were transfected with a *Wwp2* overexpression plasmid or a vector. Then, the cells were treated with CHX (catalog no. S7418, Selleck Chemicals, Houston, TX) at a concentration of 10 μ g/mL and collected at 0, 3, 6, 9, and 12 h. The time course protein levels of SDHC were monitored by western blotting.

Western blotting

Tissues and cultured cells were lysed with radioimmunoprecipitation assay buffer (catalog no. P0013B, Beyotime) supplemented with a protease inhibitor cocktail (catalog no. 04693132001, Roche, Laval, Canada). The protein concentration of the lysates was quantified with a bicinchoninic acid protein assay kit (catalog no. P0010, Beyotime). Equal amounts of protein (30–50 μ g) from each sample were subjected to SDS-PAGE and electroblotted onto polyvinylidene fluoride membranes (Bio-Rad, Hercules, CA). The membranes were then blocked in 5% nonfat milk, probed with primary antibodies, and incubated with HRP-conjugated secondary antibodies. The immunoreactive bands were visualized with HRP substrate (catalog no. P0018S, Beyotime) using the ChemiDoc XRS+ system (Bio-Rad). The following antibodies were used for western blotting: WWP2 (1:1,000, catalog no. 12197-1-AP, ProteinTech), SDHC (1:1,000, catalog no. ab155999, Abcam), NDUFA12 (1:1,000, catalog no. ER 60883, Huabio, Hangzhou, China), ATP5F1B (1:1,000, catalog no. HA601353, Huabio), p-H₂AX (1:1,000, catalog no. 9718, Cell Signaling Technology), SDHB (1:2,000, catalog no. ab14714, Abcam), NDUFB8 (1:2,000, catalog no. ab110242, Abcam), UQCRC2 (1:1,000, catalog no. ab14745, Abcam), ATP5A (1:2,000, catalog no. ab14748, Abcam), COX1 (1:1,000, catalog no. 14705, Abcam), FN (1:1,000, catalog no. ab2413, Abcam), VIM (1:1,000, catalog no. ab92547, Abcam), ACTA2 (1:5,000, catalog no. ET1607-53, Huabio), E-Cad (1:1,000, catalog no. 20874-1-AP, ProteinTech), Ki-67 (1:500, catalog no. AF1738, Beyotime), Porins (2 μ g/mL, catalog no. ab14734, Abcam), NGAL (1:3,000, catalog no. ab63929, Abcam), glyceraldehyde 3-phosphate

dehydrogenase (1:5,000, catalog no. 60004-1-Ig, ProteinTech), β -actin (1:2,000, catalog no. 66009-1-Ig, ProteinTech), COXIV (1:1,000, catalog no. 11242-1-AP, ProteinTech), Lambin B1 (1:1,000, catalog no. ET1606-27, Huabio) and Histone H3 (1:1,000, catalog no. 17168-1-AP, ProteinTech).

IP

mPTCs were co-transfected with mouse *Wwp2*-FLAG and *Sdhc*-His plasmids with PolyJet In Vitro DNA Transfection Reagent (catalog no. SL100688; SignaGen Laboratories). The cell lysate was prepared with NP40 lysis buffer (catalog no. P0013F, Beyotime) containing protease inhibitors (catalog no. 04693132001, Roche). IP was conducted by incubating the cell lysate with an antibody and protein A/G magnetic beads (catalog no. B23201; Bimake, Shanghai, China) overnight at 4°C. The immunoprecipitated proteins were eluted and analyzed by western blotting. The following antibodies were used for IP: anti-FLAG (catalog no. F3165, Sigma-Aldrich), anti-His (catalog no. 12698S, Cell Signaling Technology), anti-SDHC (catalog no. A21040, ABclonal), normal mouse IgG (catalog no. sc-2025, Santa Cruz Biotechnology, Santa Cruz, CA), and normal rabbit IgG (catalog no. 2729S, Cell Signaling Technology).

Cytoflow analysis of the cellular mtROS level and the MMP

mPTCs were digested with trypsin and harvested via centrifugation. The mtROS level was measured by incubating the cells with the superoxide indicator MitoSOX Red (catalog no. M36008; Invitrogen, Carlsbad, CA). MMP was determined by incubating the cells with the potentiometric fluorescent dye tetramethylrhodamine methyl ester (catalog no. I34361; Invitrogen). The fluorescence intensity was measured using a CytoFLEX flow cytometer (Beckman Coulter Life Sciences, Nyon, Switzerland).

Complex II activity assay

Complex II activity within cells was estimated using a commercial complex II activity assay kit (catalog no. GMS10103.1; GENMED Scientifics, Shanghai, China). Briefly, cell lysates were prepared on ice with GENMED lysis buffer. We prepared 150 μ L GENMED buffer, 20 μ L GENMED reaction solution, and 10 μ L GENMED substrate solution in a 96-well plate, following the manufacturer's instructions. Cell lysate was added to the prepared solution and immediately subjected to absorbance measurement. The absorbance of each sample was measured at a wavelength of 600 nm every 60 s for 6 cycles. Enzyme activity was calculated according to the manufacturer's instructions and normalized to protein concentration.

Measurement of succinate concentrations

Succinate concentrations in the cell medium were quantified using a commercial assay kit (catalog no. MAK335, Sigma-Aldrich). The reactions were carried out according to the manufacturer's instructions. The absorbance of each sample was then measured at 570 nm.

ATP measurement

ATP content was analyzed using a luciferase-based bioluminescence-enhanced ATP assay kit (catalog no. S0027, Beyotime). Briefly, the

treated cells were lysed on ice with the provided ATP lysis, followed by centrifugation at 12,000 $\times g$ for 5 min at 4°C. A 20- μ L cell lysate was mixed with 100 μ L freshly prepared ATP detection solution in a 96-well plate, according to the manufacturer's instructions. The luminescence intensity was measured by the Luciferase Reporter Assay System (Promega, Madison, WI). ATP levels were normalized to protein concentrations.

Enzyme-linked immunosorbent assay of Cyto C release

The concentration of Cyto C in the cell culture media was determined with an enzyme-linked immunosorbent assay (ELISA) kit (catalog no. ml001967, Mlbio, Shanghai, China). We collected and incubated 100 μ L cell culture supernatant in a 96-well plate with a primary antibody solution for 1.5 h at 37°C, followed by washing per the manufacturer's instructions. We then added 100 μ L biotinylated antibody working solution to each well and incubated it for 1 h at 37°C. After incubation with an enzyme conjugate working solution for 30 min, chromogen solutions A and B were added to each well. The reaction was terminated with a stop solution. The absorbance of each sample was then measured at 450 nm.

Protein-protein docking

The structures of the HECT domain of WWP2 (PDB: 4Y07) and the complex II (PDB: 8GS8) were prepared with Schrödinger's Protein Preparation Wizard. Protein-protein docking was then carried out with WWP2 as the receptor and complex II as the ligand via PIPER. The docked 3D protein-protein complex was generated by Maestro.

Virtual screening

The structure of the HECT domain of WWP2 (PDB: 4Y07) was prepared with Schrödinger's Protein Preparation Wizard as the receptor for virtual screening. The small-molecule database used for virtual screening was the Maybridge Hitfinder database (Trevillett, UK), with 14,400 bioactive compounds in total. The compounds were prepared and docked into the receptor at standard precision via Glide. The docked 3D and 2D ligand-protein complexes were generated by Maestro.

WWP2 ubiquitylation enzyme activity assay

The ubiquitylation reaction mixture contained 40 mM Tris-HCl (pH 7.6), 2 mM dithiothreitol, 2 mM MgCl₂, 0.2 μ g UBE1 (catalog no. E-304-050, R&D Systems, Minneapolis, MN), 0.2 μ g UBE2D2 (catalog no. E2-620-100, R&D Systems), 0.2 μ g WWP2-GST protein (produced and purified from *Escherichia coli*), and 1 μ g FLAG-tagged ubiquitin (catalog no. U5382, Sigma-Aldrich). The compounds were preincubated with the reaction mixture for 30 min at 37°C before 0.6 μ g of the substrate protein PTEN (catalog no. ab157087, Abcam) and 2.5 mM ATP (catalog no. A1852, Sigma-Aldrich) were added to initiate the ubiquitination reaction. The reactions were terminated after 30 min by adding 5 \times SDS buffer (catalog no. P0015, Beyotime) and boiling for 5 min. The protein mixture was analyzed by western blotting, and the ubiquitin level was

estimated by incubation with an anti-FLAG antibody (1:1,000, catalog no. F3165, Sigma-Aldrich).

BLI analysis

The binding affinities of WWP2 for compounds H36-E4 and H111-H7 were determined using the GatorPlus BLI system (Gator Bio, Palo Alto, CA). All steps were performed at 30°C and 1,000 rpm. Briefly, anti-GST sensors (catalog no. 160042, GatorBio) were dipped into WWP2-GST protein solutions for 15 min for loading and then dipped into various concentrations of H36-E4 (2–5.2 μM) and H111-H7 (12.5–1,000 nM) in PBS/0.02% Tween 20/0.1% DMSO buffer. Background binding controls used duplicate sensors incubated in a buffer without proteins. All the data were analyzed using Gator Bio data analysis software. The equilibrium K_D values were calculated from the ratio of K_{off} to K_{on} according to the global fitting of several curves generated from serial dilutions of the compounds.

RNA-seq

Kidney tissues were collected from WT and WWP2 PT^{CKO} mice constructed with or without the UIR model for 21 days. The Beijing Genomic Institution performed RNA extraction and RNA expression profiling using the BGISEQ-500 RNA-sequencing (RNA-seq) platform. Differentially expressed genes were defined as those with a fold change ≥ 1.2 and a $q < 0.05$. Kyoto Encyclopedia of Genes and Genomes (KEGG) and GO enrichment analyses were performed using the online tool provided by the Beijing Genomics Institute (<https://biosys.bgi.com>).

Statistical analysis

Statistical analyses were performed with GraphPad Prism 10 (GraphPad Software, San Diego, CA). The data are presented as the means \pm SEMs. The unpaired Student's t test (two-tailed) was used to assess the statistical significance of differences between two groups. One-way ANOVA was used to analyze differences between multiple groups with one variable, and two-way ANOVA was used to compare multiple groups with more than one variable. $p < 0.05$ was considered to indicate significance: * $p < 0.05$; ** $p < 0.01$; *** $p < 0.001$; **** $p < 0.0001$.

DATA AND CODE AVAILABILITY

The ubiquitylation-omics and proteomics data supporting the findings of our study have been deposited to the ProteomeXchange Consortium (ProteomeXchange: PXD048540 and PXD048622). Raw data files and processed data of transcriptional analyses of kidney tissues have been submitted to the database of NCBI Gene Expression Omnibus (GEO) (GEO: GSE293589, secure token number: glaruwqznzuxot). Other data that support the findings of this study are available on request to the corresponding authors.

ACKNOWLEDGMENTS

This work was supported by the National Key Technologies Research and Development Program of China (2022YFC2705100, 2022YFC2705105, and 2022YFC2705102), National Natural Science Foundation grants of China (82470723, 82090022, 82270773, 82170688, 82170754, and W2411073), the Natural Science Foundation of Jiangsu Province (BK20231130), the Medical Research Project from Jiangsu Health Commission (Z2020271), the Outstanding Youth Project from Nanjing Health Commission (JQX22010), and the Postgraduate Research & Practice Innovation Program of Jiangsu Province (JX12214362, JX12214204, and JX12214135).

AUTHOR CONTRIBUTIONS

Conceptualization, A.Z., Z.J., and M.W.; methodology, M.W., M.M., Y.L., J.F., W.Z., Y.N., R.L., W.C., and R.Z.; investigation, M.W., M.M., Y.L., and J.F.; visualization, M.W., M.M., Y.L., and J.F.; funding acquisition, A.Z., Z.J., M.W., S.H., Y.Z., M.M., Y.L., and W.Z.; project administration, A.Z., Z.J., R.Y., M.B., Y.Z., and S.H.; supervision, A.Z., Z.J., Y.Z., and S.H.; writing – original draft, M.W., M.M., and Y.L.; writing – review & editing, Z.J., A.Z., R.Y., and M.B.

DECLARATION OF INTERESTS

The authors declare no competing interests.

SUPPLEMENTAL INFORMATION

Supplemental information can be found online at <https://doi.org/10.1016/j.ymthe.2025.11.022>.

REFERENCES

- Kellum, J.A., Romagnani, P., Ashuntantang, G., Ronco, C., Zarbock, A., and Anders, H.J. (2021). Acute kidney injury. *Nat. Rev. Dis. Primers* 7, 52. <https://doi.org/10.1038/s41572-021-00284-z>.
- Liu, Y. (2024). Kidney fibrosis: fundamental questions, challenges, and perspectives. *Integr. Med. Nephrol. Androl.* 11, e24–e27. <https://doi.org/10.1097/imna-d-24-00027>.
- Romagnani, P., Remuzzi, G., Glasscock, R., Levin, A., Jager, K.J., Tonelli, M., Massy, Z., Wanner, C., and Anders, H.J. (2017). Chronic kidney disease. *Nat. Rev. Dis. Primers* 3, 17088. <https://doi.org/10.1038/nrdp.2017.88>.
- Liu, B.C., Tang, T.T., Lv, L.L., and Lan, H.Y. (2018). Renal tubule injury: a driving force toward chronic kidney disease. *Kidney Int.* 93, 568–579. <https://doi.org/10.1016/j.kint.2017.09.033>.
- Kusaba, T., Lalli, M., Kramann, R., Kobayashi, A., and Humphreys, B.D. (2014). Differentiated kidney epithelial cells repair injured proximal tubule. *Proc. Natl. Acad. Sci. USA* 111, 1527–1532. <https://doi.org/10.1073/pnas.1310653110>.
- Kirita, Y., Wu, H., Uchimura, K., Wilson, P.C., and Humphreys, B.D. (2020). Cell profiling of mouse acute kidney injury reveals conserved cellular responses to injury. *Proc. Natl. Acad. Sci. USA* 117, 15874–15883. <https://doi.org/10.1073/pnas.2005477117>.
- Aggarwal, S., Wang, Z., Rincon Fernandez Pacheco, D., Rinaldi, A., Rajewski, A., Callemeyn, J., Van Loon, E., Lamarthée, B., Covarrubias, A.E., Hou, J., et al. (2024). SOX9 switch links regeneration to fibrosis at the single-cell level in mammalian kidneys. *Science* 383, eadd6371. <https://doi.org/10.1126/science.add6371>.
- Zhu, M., Zhang, Z., Chen, Z., Xu, Y., Wu, J., Che, X., Ying, L., Shao, X., Tang, L., Zhou, W., et al. (2022). Single-cell RNA landscape of cell fate decision of renal proximal tubular epithelial cells and immune-microenvironment in kidney fibrosis. *Clin. Transl. Med.* 12, e1010. <https://doi.org/10.1002/ctm2.1010>.
- Szeto, H.H. (2017). Pharmacologic approaches to improve mitochondrial function in AKI and CKD. *J. Am. Soc. Nephrol.* 28, 2856–2865. <https://doi.org/10.1681/asn.2017030247>.
- Xu, X., Zhu, W., Miao, M., Bai, M., Fan, J., Niu, Y., Li, Y., Zhang, A., Jia, Z., and Wu, M. (2024). Activation of LONP1 by 84-B10 alleviates aristolochic acid nephropathy via re-establishing mitochondrial and peroxisomal homeostasis. *Chin. J. Nat. Med.* 22, 808–821. [https://doi.org/10.1016/s1875-5364\(24\)60608-4](https://doi.org/10.1016/s1875-5364(24)60608-4).
- Lan, R., Geng, H., Singha, P.K., Saikumar, P., Bottinger, E.P., Weinberg, J.M., and Venkatachalam, M.A. (2016). Mitochondrial pathology and glycolytic shift during proximal tubule atrophy after ischemic AKI. *J. Am. Soc. Nephrol.* 27, 3356–3367. <https://doi.org/10.1681/asn.2015020177>.
- Li, X., Chen, J., Li, J., Zhang, Y., Xia, J., Du, H., Sheng, C., Huang, M., Shen, W., Cai, G., et al. (2025). ATGL regulates renal fibrosis by reprogramming lipid metabolism during the transition from AKI to CKD. *Mol. Ther.* 33, 805–822. <https://doi.org/10.1016/j.ymthe.2024.12.053>.
- Ma, F.Y., Tesch, G.H., Grynberg, K., Ozols, E., Mulley, W.R., and Nikolic-Paterson, D.J. (2023). A model of ischaemia-induced renal interstitial fibrosis in mice with established diabetes. *Integr. Med. Nephrol. Androl.* 10, e00032. <https://doi.org/10.1097/imna-d-22-00032>.

14. Caron, P., Pankotai, T., Wiegant, W.W., Tollenaere, M.A.X., Furst, A., Bonhomme, C., Helfricht, A., de Groot, A., Pastink, A., Vertegaal, A.C.O., et al. (2019). WWP2 ubiquitylates RNA polymerase II for DNA-PK-dependent transcription arrest and repair at DNA breaks. *Genes Dev.* 33, 684–704. <https://doi.org/10.1101/gad.321943.118>.
15. Zhang, N., Zhang, Y., Wu, B., You, S., and Sun, Y. (2020). Role of WW domain E3 ubiquitin protein ligase 2 in modulating ubiquitination and Degradation of Septin4 in oxidative stress endothelial injury. *Redox Biol.* 30, 101419. <https://doi.org/10.1016/j.redox.2019.101419>.
16. Chen, A., Gao, B., Zhang, J., McEwen, T., Ye, S.Q., Zhang, D., and Fang, D. (2009). The HECT-type E3 ubiquitin ligase AIP2 inhibits activation-induced T-cell death by catalyzing EGR2 ubiquitination. *Mol. Cell. Biol.* 29, 5348–5356. <https://doi.org/10.1128/mcb.00407-09>.
17. Lu, X., Huang, X., Xu, H., Lu, S., You, S., Xu, J., Zhan, Q., Dong, C., Zhang, N., Zhang, Y., et al. (2022). The role of E3 ubiquitin ligase WWP2 and the regulation of PARP1 by ubiquitinated degradation in acute lymphoblastic leukemia. *Cell Death Discov.* 8, 421. <https://doi.org/10.1038/s41420-022-01209-9>.
18. Zhang, Z., Lu, Y.X., Liu, F., Sang, L., Shi, C., Xie, S., Bian, W., Yang, J.C., Yang, Z., Qu, L., et al. (2023). lncRNA BREA2 promotes metastasis by disrupting the WWP2-mediated ubiquitination of Notch1. *Proc. Natl. Acad. Sci. USA* 120, e2206694120. <https://doi.org/10.1073/pnas.2206694120>.
19. Chen, H., Chew, G., Devapragash, N., Loh, J.Z., Huang, K.Y., Guo, J., Liu, S., Tan, E.L.S., Chen, S., Tee, N.G.Z., et al. (2022). The E3 ubiquitin ligase WWP2 regulates pro-fibrogenic monocyte infiltration and activity in heart fibrosis. *Nat. Commun.* 13, 7375. <https://doi.org/10.1038/s41467-022-34971-6>.
20. You, S., Xu, J., Yin, Z., Wu, B., Wang, P., Hao, M., Cheng, C., Liu, M., Zhao, Y., Jia, P., et al. (2023). Down-regulation of WWP2 aggravates Type 2 diabetes mellitus-induced vascular endothelial injury through modulating ubiquitination and degradation of DDX3X. *Cardiovasc. Diabetol.* 22, 107. <https://doi.org/10.1186/s12933-023-01818-3>.
21. Zhao, Z.B., Marschner, J.A., Iwakura, T., Li, C., Motrapu, M., Kuang, M., Popper, B., Linkermann, A., Klocke, J., Enghard, P., et al. (2023). Tubular epithelial cell HMGB1 promotes AKI-CKD transition by sensitizing cycling tubular cells to oxidative stress: A rationale for targeting HMGB1 during AKI recovery. *J. Am. Soc. Nephrol.* 34, 394–411. <https://doi.org/10.1681/asn.0000000000000024>.
22. Wu, M., Chen, W., Miao, M., Jin, Q., Zhang, S., Bai, M., Fan, J., Zhang, Y., Zhang, A., Jia, Z., and Huang, S. (2021). Anti-anemia drug FG4592 retards the AKI-to-CKD transition by improving vascular regeneration and antioxidative capability. *Clin. Sci.* 135, 1707–1726. <https://doi.org/10.1042/cs20210100>.
23. You, R., Li, Y., Jiang, Y., Hu, D., Gu, M., Zhou, W., Zhang, S., Bai, M., Yang, Y., Zhang, Y., et al. (2025). WWP2 deletion aggravates acute kidney injury by targeting CDC20/autophagy axis. *J. Adv. Res.* 71, 471–485. <https://doi.org/10.1016/j.jare.2024.06.015>.
24. Backes, S., Hess, S., Boos, F., Woellhaf, M.W., Gödel, S., Jung, M., Mühlhaus, T., and Herrmann, J.M. (2018). Tom70 enhances mitochondrial preprotein import efficiency by binding to internal targeting sequences. *J. Cell Biol.* 217, 1369–1382. <https://doi.org/10.1083/jcb.201708044>.
25. Boos, F., Mühlhaus, T., and Herrmann, J.M. (2018). Detection of internal matrix targeting signal-like sequences (iMTS-Ls) in mitochondrial precursor proteins using the targetP prediction tool. *Bio. Protoc.* 8, e2474. <https://doi.org/10.21769/BioProtoc.2474>.
26. Zhang, Y., Yang, Y., Yang, F., Liu, X., Zhan, P., Wu, J., Wang, X., Wang, Z., Tang, W., Sun, Y., et al. (2023). HDAC9-mediated epithelial cell cycle arrest in G2/M contributes to kidney fibrosis in male mice. *Nat. Commun.* 14, 3007. <https://doi.org/10.1038/s41467-023-38771-4>.
27. Turner, N.A. (2016). Inflammatory and fibrotic responses of cardiac fibroblasts to myocardial damage associated molecular patterns (DAMPs). *J. Mol. Cell. Cardiol.* 94, 189–200. <https://doi.org/10.1016/j.jmcc.2015.11.002>.
28. Rajesh, R., Mooslechner, A.A., Schweighofer, H., Pahernik, S., Lanz, I., Atallah, R., Platzer, W., Aigner, C., Benazzo, A., Angiari, S., et al. (2025). Succinate aggravates pulmonary fibrosis through the succinate/SUCNR1 axis. *Am. J. Physiol. Lung Cell. Mol. Physiol.* 328, L671–L684. <https://doi.org/10.1152/ajplung.00286.2024>.
29. Khazal, F.A., Holte, M.N., Bolon, B., White, T.A., LeBrasseur, N., and Iii, L.J.M. (2019). A conditional mouse model of complex II deficiency manifesting as Leigh-like syndrome. *FASEB J.* 33, 13189–13201. <https://doi.org/10.1096/fj.201802655RR>.
30. Chen, H., You, R., Guo, J., Zhou, W., Chew, G., Devapragash, N., Loh, J.Z., Gesualdo, L., Li, Y., Jiang, Y., et al. (2024). WWP2 regulates renal fibrosis and the metabolic reprogramming of profibrotic myofibroblasts. *J. Am. Soc. Nephrol.* 35, 696–718. <https://doi.org/10.1681/asn.0000000000000328>.
31. Wu, M., Jin, Q., Xu, X., Fan, J., Chen, W., Miao, M., Gu, R., Zhang, S., Guo, Y., Huang, S., et al. (2023). TP53RK drives the progression of chronic kidney disease by phosphorylating Birc5. *Adv. Sci.* 10, e2301753. <https://doi.org/10.1002/adv.202301753>.
32. Scott, R.P., and Quaggin, S.E. (2015). Review series: The cell biology of renal filtration. *J. Cell Biol.* 209, 199–210. <https://doi.org/10.1083/jcb.201410017>.
33. Bezawork-Geleta, A., Rohlena, J., Dong, L., Pacak, K., and Neuzil, J. (2017). Mitochondrial complex II: At the crossroads. *Trends Biochem. Sci.* 42, 312–325. <https://doi.org/10.1016/j.tibs.2017.01.003>.
34. Bai, M., Wu, M., Jiang, M., He, J., Deng, X., Xu, S., Fan, J., Miao, M., Wang, T., Li, Y., et al. (2023). LONP1 targets HMGCs2 to protect mitochondrial function and attenuate chronic kidney disease. *EMBO Mol. Med.* 15, e16581. <https://doi.org/10.15252/emmm.202216581>.
35. Zhang, L., Miao, M., Xu, X., Bai, M., Wu, M., and Zhang, A. (2023). From physiology to pathology: The role of mitochondria in acute kidney injuries and chronic kidney diseases. *Kidney Dis.* 9, 342–357. <https://doi.org/10.1159/000530485>.
36. Fan, J., Xu, X., Li, Y., Zhang, L., Miao, M., Niu, Y., Zhang, Y., Zhang, A., Jia, Z., and Wu, M. (2023). A novel 3-phenylglutaric acid derivative (84-B10) alleviates cisplatin-induced acute kidney injury by inhibiting mitochondrial oxidative stress-mediated ferroptosis. *Free Radic. Biol. Med.* 194, 84–98. <https://doi.org/10.1016/j.freeradbiomed.2022.11.029>.
37. Busch, J.D., Fielden, L.F., Pfanner, N., and Wiedemann, N. (2023). Mitochondrial protein transport: Versatility of translocases and mechanisms. *Mol. Cell* 83, 890–910. <https://doi.org/10.1016/j.molcel.2023.02.020>.
38. Watt, J.E., Hughes, G.R., Walpole, S., Monaco, S., Stephenson, G.R., Bulman Page, P.C., Hemmings, A.M., Angulo, J., and Chantray, A. (2018). Discovery of small molecule WWP2 ubiquitin ligase inhibitors. *Chemistry* 24, 17677–17680. <https://doi.org/10.1002/chem.201804169>.
39. Tannahill, G.M., Curtis, A.M., Adamik, J., Palsson-McDermott, E.M., McGettrick, A.F., Goel, G., Frezza, C., Bernard, N.J., Kelly, B., Foley, N.H., et al. (2013). Succinate is an inflammatory signal that induces IL-1 β through HIF-1 α . *Nature* 496, 238–242. <https://doi.org/10.1038/nature11986>.
40. Pu, M., Zhang, J., Hong, F., Wang, Y., Zhang, C., Zeng, Y., Fang, Z., Qi, W., Yang, X., Gao, G., and Zhou, T. (2024). The pathogenic role of succinate-SUCNR1: a critical function that induces renal fibrosis via M2 macrophage. *Cell Commun. Signal.* 22, 78. <https://doi.org/10.1186/s12964-024-01481-5>.
41. Eleftheriadis, T., Pissas, G., Liakopoulos, V., and Stefanidis, I. (2016). Cytochrome c as a Potentially Clinical Useful Marker of Mitochondrial and Cellular Damage. *Front. Immunol.* 7, 279. <https://doi.org/10.3389/fimmu.2016.00279>.
42. Su, H., Ye, C., Lei, C.T., Tang, H., Zeng, J.Y., Yi, F., and Zhang, C. (2020). Subcellular trafficking of tubular MDM2 implicates in acute kidney injury to chronic kidney disease transition during multiple low-dose cisplatin exposure. *FASEB J.* 34, 1620–1636. <https://doi.org/10.1096/fj.201901412R>.
43. Xu, X., Miao, M., Zhu, W., Zhang, L., Jin, Q., Li, Y., Xu, M., Jia, Z., Zhang, A., and Wu, M. (2025). Interferon regulatory factor 5 attenuates kidney fibrosis through transcriptional suppression of Tgfb β 1. *Int. Immunopharmacol.* 148, 114031. <https://doi.org/10.1016/j.intimp.2025.114031>.